PHILOSOPHICAL TRANSACTIONS A

royalsocietypublishing.org/journal/rsta

Research

Cite this article: Alsulami OZ, Alahmadi AA, Saeed SOM, Mohamed SH, El-Gorashi TEH, Alresheedi MT, Elmirghani JMH. 2020 Optimum resource allocation in optical wireless systems with energy-efficient fog and cloud architectures. *Phil. Trans. R. Soc. A* **378**: 20190188.
http://dx.doi.org/10.1098/rsta.2019.0188

Accepted: 6 January 2020

One contribution of 17 to a theme issue 'Optical wireless communication'.

Subject Areas:
electrical engineering, power and energy systems

Keywords:
optical wireless communication, multi-users, data rate, power consumption, fog computing, MILP

Author for correspondence:
Osama Zwaid Alsulami
e-mail: ml15ozma@leeds.ac.uk

THE ROYAL SOCIETY PUBLISHING

Optimum resource allocation in optical wireless systems with energy-efficient fog and cloud architectures

Osama Zwaid Alsulami[1], Amal A. Alahmadi[1], Sarah O. M. Saeed[1], Sanaa Hamid Mohamed[1], T. E. H. El-Gorashi[1], Mohammed T. Alresheedi[2] and Jaafar M. H. Elmirghani[1]

[1]School of Electronic and Electrical Engineering, University of Leeds, LS2 9JT Leeds, UK
[2]Department of Electrical Engineering, King Saud University, Riyadh, Kingdom of Saudi Arabia

OZA, 0000-0002-2096-307X; AAA, 0000-0002-6371-1614; SOMS , 0000-0002-0828-7160; SHM, 0000-0002-6234-1906; JMHE , 0000-0002-3319-9103

Optical wireless communication (OWC) is a promising technology that can provide high data rates while supporting multiple users. The optical wireless (OW) physical layer has been researched extensively, however, less work was devoted to multiple access and how the OW front end is connected to the network. In this paper, an OWC system which employs a wavelength division multiple access (WDMA) scheme is studied, for the purpose of supporting multiple users. In addition, a cloud/fog architecture is proposed for the first time for OWC to provide processing capabilities. The cloud/fog-integrated architecture uses visible indoor light to create high data rate connections with potential mobile nodes. These OW nodes are further clustered and used as fog mini servers to provide processing services through the OW channel for other users. Additional fog-processing units are located in the room, the building, the campus and at the metro level. Further processing capabilities

are provided by remote cloud sites. Two mixed-integer linear programming (MILP) models were proposed to numerically study networking and processing in OW systems. The first MILP model was developed and used to optimize resource allocation in the indoor OWC systems, in particular, the allocation of access points (APs) and wavelengths to users, while the second MILP model was developed to optimize the placement of processing tasks in the different fog and cloud nodes available. The optimization of tasks placement in the cloud/fog-integrated architecture was analysed using the MILP models. Multiple scenarios were considered where the mobile node locations were varied in the room and the amount of processing and data rate requested by each OW node was varied. The results help to identify the optimum colour and AP to use for communication for a given mobile node location and OWC system configuration, the optimum location to place processing and the impact of the network architecture.

This article is part of the theme issue 'Optical wireless communication'.

1. Introduction

The increasing demand for high data rates and the increasing number of Internet-connected devices [1] will soon be beyond the capabilities of the current radio frequency spectrum. Meeting these demands requires access to new spectra that can provide high data rate connectivity. Moreover, new computing and networking architectures that support indoor fog computing resources in addition to cloud computing are needed to establish future-proof and energy-efficient networking and computing systems.

The optical spectrum is a potential solution that offers excellent indoor channel characteristics, abundant bandwidth, and can be accessed using relatively low-cost components [2–9]. Recently, many studies have shown that video, data and voice can be transmitted through optical wireless communication (OWC) systems at high data rates of up to 25 Gbps and beyond in indoor environments [8–19]. OWC multiplexing and multiple access (MA) techniques are a key requirement to support multiple users. Different configurations of transmitters and receivers, in terms of their number and directionality, have been shown to help in reducing the delay spread and increasing the signal-to-noise ratio [12,20–27]. To avoid degradation of the signal quality due to multiple users, efficient utilization of resources is necessary. Multiplexing of OWC resources including space, time, power and wavelength resources has thus, recently, attracted the attention of researchers.

With the aim of reducing service latency and power consumption of cloud computing paradigms, recent research has focused on proposing new distributed architectures and solutions to offload the processing demands from central data centres. In this respect, distributed clouds (DC) are a new generation of cloud computing, where processing tasks are 'distributed' to mini data centre locations, known as fog data centres close to the end users, resulting in faster response and decreased networking burdens. However, for this paradigm to be efficient, their distributed applications require a fast communication medium. With data rates of up to 25 Gbps and beyond [6,7], OWC systems can satisfy the needs of these distributed applications and can be viewed as a promising medium for supporting such a paradigm with indoor computing resources.

This paper proposes an indoor multiple access OWC system to be used in conjunction with cloud/fog-integrated architecture. This system creates connections with potential mobile nodes and regards them as mini fog servers that can provide processing services. To the best of our knowledge, no previous work has proposed the integration of fog computing with OWC systems. In this work, we model and optimize the indoor optical wireless (OW) system through a mixed-integer linear programme (MILP) that optimizes the allocation of access points (APs) and wavelength resources to mobile nodes so that the sum signal to interference-plus-noise ratios (SINRs) is maximized. The APs, and wavelengths MILP-based assignment is then used

to determine the achievable data rate of each mobile user. These values are then used to optimize the computing resources allocation in the fog/cloud architecture where a comprehensive MILP model is used to minimize the total computing and networking power consumption. That is, the output of the first MILP model (which consists of the supported data rates, and the assigned APs and wavelengths of each user) is used as input to the second MILP model to represent the link capacity, the node identifier in the cloud/fog architecture, and the power consumed by each wavelength, respectively. This paper thus considers the optimum allocation of resources in OW systems, where the resources can be related to the physical layer, or can be related to the network layer. It is essential to treat the resource allocation problem in a unified single treatment as this ensures that the optimum solution to one problem does not compromise other parts of the network. We believe that our treatment is the first to attempt this goal and has achieved an important first step in this direction.

The rest of this paper is organized as follows: §2 reviews MA techniques in OWC, fog computing and distributed processing. MILP optimization of resource allocation in OW systems is discussed in §3. Section 4 describes the optimum placement of processing to minimize power consumption, and §5 presents the conclusions.

2. Literature review

(a) Multiple access schemes in optical wireless communication

MA schemes have been considered for application in OWC systems. Some of the MA schemes used in RF systems are also used in OWC systems. Well-known MA schemes in OWC systems include time division multiple access, frequency division multiple access (FDMA), code division multiple access, space division multiple access, non-orthogonal multiple access and wavelength division multiple access (WDMA).

In this work, WDMA is used for multiple access. WDMA can support multiple users based on wavelength division multiplexing (WDM). It has been studied in OWC systems [5,28–32]. WDMA uses a multiplexer at the transmitter for aggregating different wavelengths from different light sources into a single OW beam. Thereafter, at the receiver, a de-multiplexer is used to separate the wavelengths, thus supporting MA. The operation of WDMA is similar to that of FDMA, with both operating in the frequency domain. The two light sources typically used in OWC systems (LEDs and LDs) were investigated in [31,32]. When using red, green and blue (RGB) LEDs (figure 1*a*), a data rate of more than 3.22 Gbps was achieved in [31] through WDMA implementation in a visible light communication (VLC) system. Moreover, another demonstration of a VLC system that used WDMA was reported in [32]. In addition, by using red, yellow, green and blue (RYGB) LDs (figure 1*b*), the researchers in [5] achieved a data rate of up to 10 Gbps.

(b) Fog computing and distributed processing

The vast expansion in the usage of cloud services, and the significant increase in distributed services, call for new architectures and solutions to provision those services at high data rates to the end user while reducing latency and power consumption. Distributed computing has become a popular solution that shifts the workload from the central cloud to the fog and, thus, closer to end users; hence, DC technology was developed to provide access to computational resources at the edge of the network, in close proximity to the end user, instead of accessing the central cloud. This has resulted in faster services and lower computing burdens, thereby minimizing central data centre power consumption, and reducing the overall power consumption and latency. Proposed and tested architectures that accommodate the concept and features of DC are referred to as 'cloudlets' [33], 'fog' [34] or 'edge computing' [35]. Processing at the edge nodes, and the networking fabric used to enable this, are considered to be major attributes of fog architectures.

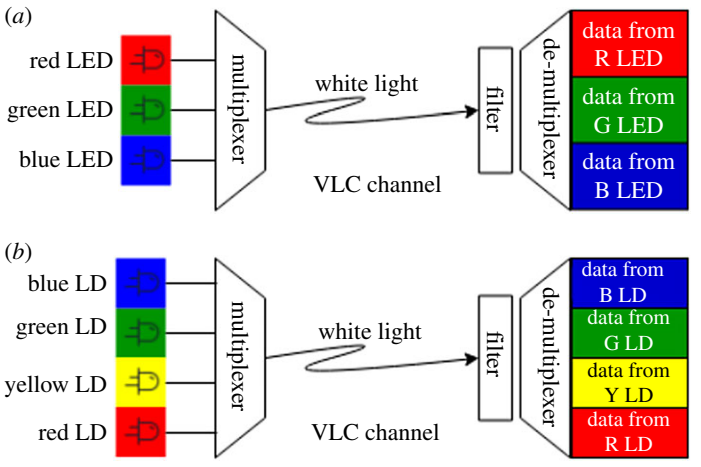

Figure 1. WDM used in VLC systems (*a*) using LEDs and (*b*) using LDs. (Online version in colour.)

These attributes play an important role in delivering a service with lower latency and power consumption.

The type of edge nodes affects the performance of the processing task and, therefore, the delivery of the requested services. Building small distributed data centres, using a smaller number of high-performance servers [36], has been proven to deliver good throughput with lower power consumption and latency. A newer approach aims to build a cluster of fog nodes out of underutilized computing resources in computer clusters [37]. This approach has led to a new definition of the type of fog nodes that can be used as processing nodes. With the huge expansion in the number of smart devices and IoT, fog can comprise any smart devices clustered as a single fog mini data centre to provide processing services. Such a paradigm is built from available idle or underutilized resources that become available opportunistically. This leads to new fog frameworks that can make use of IoT nodes [38,39], smartphones [40] and any other portable devices [41]. Recently, smartphones have become a very promising candidate as an edge processing unit. This is because of the recent rapid increase in their processing and communication capabilities. Many researches have proposed scenarios to evaluate and optimize task offloading in the mobile devices. An example of such efforts was presented by Miluzzo *et al*. [40] where a vision of mobile devices as a core for the cloudlet-distributed processing was proposed and evaluated. Another study proposed by Chen *et al*. [42] tackled the problem of the mobile devices energy consumption optimization during task offloading processes. The processing and communication problem is formulated as a cost optimization problem, considering the effect of delay on offloaded tasks. Same delay problems were tackled in [43], where processing and communication completion time for mobile applications were compared in situations where applications are allocated to mobile or central clouds.

The networking fabric also plays an important role in fog-based architectures. Fabrics with high data-rate communication enhance the connection between the end user and fog nodes, and thereby achieve improved service delivery. Communication technologies that can support fog-based computing can be found in [42]. Optical communication has been shown to satisfy the required data rate for distributed mini data centres [44]. Since most of the edge smart devices are equipped with wireless/cellular networking capabilities, these are the two main mediums currently supporting end user connections to opportunistic fog nodes. However, with the recent huge expansion of services and application demands, these mediums may not support the required data rates needed. This calls for more research into the application of high data-rate

mediums, such as wired fibre-optics, wired visible light communication, wireless visible light communication and OW communication in fog-based networks. This paper provides the first study to the best of our knowledge where OW systems are considered and integrated with opportunistic and fixed fog nodes considering the OW systems resource allocation mechanisms needed and the optimum placement of processing jobs all the way from the OW system handset/mobile unit to the central cloud passing through different fixed fog options at the room, building, campus and metro levels.

3. Mixed-integer linear programming optimization for resource allocation in OW systems

WDM can be used in both the uplink and downlink of OWC systems. In VLC systems, wavelengths in the visible light range can be optically summed to form the white light used in illumination and communication, as in [30] where four-colour (RYGB) LDs were used. In the uplink, to avoid the problem of glare, infrared uplink design was proposed in [45,46]. In this study, only the downlink will be considered. A controller, which can be located in the optical line terminal (OLT) in the room, is assumed to have knowledge of the user's location and hence their channel information using, for example, VLC localization, as in our work in [47]. This controller responds to the slow movement of people in the indoor environment and changes the resource allocation accordingly. We assumed a room with dimensions as shown in table 1, in which the parameters of the transmitter and receiver are also given. An angle diversity receiver (ADR) similar to [8] was used in this work.

Three eight-users scenarios with fixed user locations were considered. The first scenario was chosen as the worst-case scenario in terms of SINR where the four wavelengths of the AP were assigned to four users. This results in the worst-case scenario as the green and blue wavelengths are used. These wavelengths have the lowest powers and this is reflected in terms of the lower overall supported data rates. The third scenario was chosen as the best possible scenario where each AP just serves one user. Here, the AP uses its best colour/wavelength, which is the red wavelength as this has the highest power. In the second scenario, users were distributed over the room where each AP just assigned the two best wavelengths to users (red and yellow), which is the middle scenario between scenarios 1 and 3. The channel was characterized using a simulation package similar to that in [49,50]. Up to the second reflections were considered in this work as higher-order reflections have no significant impact on the received power [49,50]. The channel impulse response was then used to calculate the delay spread and the optical channel bandwidth using the parameters in table 1.

The cumulative distribution function for the optical channel bandwidth composed using 128 locations in the room is shown in figure 2. It can be seen that around 80% of the locations in the room support a bandwidth of at least 5.5 GHz. This was achieved by using the ADR, thus, reducing the field of view (FOV) of the receiver to limit the number of input rays, which results in decreasing the delay spread and hence increasing the bandwidth.

A MILP model was developed to optimize WDM wavelength assignment to maximize the sum of SINRs for all users [47]. The precalculated values of the channel impulse response were used to calculate the optical power received at each potential location in the room from each AP using different wavelengths. The MILP model was then used to assign APs and wavelengths to users so that the sum of SINRs was maximized, based on optical channel information. Figure 3 illustrates a scenario with three users. Users 1 and 2 suffer from background light shot noise in addition to interference as they are assigned the red wavelength, while user 3 suffers only from background light shot noise as the green wavelength is not assigned to other users.

Before introducing the MILP model, we define the sets, parameters and variables used, and describe how the SINR is calculated

Sets:	
$\mathcal{U}$	set of users in the room;
$\mathcal{A}$	set of access points;
$\mathcal{W}$	set of available wavelengths (RYGB);
$\mathcal{B}$	set of receiver branches (faces);
parameters:	
u, m	user indices; u is desired user, m indexes other users who may cause interference;
a, b	access point indices; a is the access point allocated to user u, b is an access point allocated to another user m;
λ	wavelength index;
f, g	receiver face (branch), for the desired user and the other users;
$PO_{u,f}^{a,\lambda}$	optical power received by user u from an access point a using wavelength λ and branch f. This value was precalculated using a channel modelling tool, where the line of sight and first-order reflection components were calculated for the given access point and user location and for the given wavelengths on each branch;
$P_{u,f}^{a,\lambda}$	the squared electrical current at the receiver of user u due to the optical power received from access point a at the wavelength λ on receiver branch f. (Note that the squared current and electrical power are equivalent for a given system input impedance);
$\sigma_{u,f}^{b,\lambda}$	the shot noise mean square current at the receiver of user u due to the background unmodulated power of access point b operating at wavelength λ on receiver branch f;
σ_{Rx}	the mean square receiver noise current;
variables:	
$\gamma_{u,f}^{a,\lambda}$	SINR of user u assigned to access point a and wavelength λ using branch f of the receiver;
$S_{u,f}^{a,\lambda}$	a selector function where a binary value of 1 indicates the assignment of user u to access point a and wavelength λ (figure 3) and received through branch f of the receiver;
$\phi_{m,u,f}^{a,b,\lambda}$	non-negative linearization variable, where $\phi_{m,u,f}^{a,b,\lambda} = \gamma_{u,f}^{a,\lambda} S_{m,g}^{b,\lambda}$.

To calculate the SINR, different powers are calculated as follows:

The electrical signal power received by user u from AP a and using wavelength λ on branch f is calculated as

$$P_{u,f}^{a,\lambda} = (RPt_{u,f}^{a,\lambda} h_{u,f}^{a,\lambda})^2, \tag{3.1}$$

where R is the responsivity of the photodetector in (A/W), $Pt_{u,f}^{a,\lambda}$ is the optical power transmitted by the AP a allocated to the user u using wavelength λ received through branch f and $h_{u,f}^{a,\lambda}$ is the DC channel gain between AP a and user u for wavelength λ through branch f.

The preamplifier noise is given by

$$\sigma_{Rx} = N_{\mathrm{pr}} B_e, \tag{3.2}$$

where N_{pr} is the preamplifier noise power density in (A^2/Hz) and B_e is the electrical bandwidth.

The background light shot noise is calculated as

$$\sigma_{u,f}^{b,\lambda} = 2e(RPt_{u,f}^{b,\lambda} h_{u,f}^{b,\lambda}) B_o B_e, \tag{3.3}$$

where e is the electron charge and B_o is the optical bandwidth, where the shot noise is attributed to unmodulated light sources, with the optical filter bandwidth set to 1 to avoid rejecting desired signals that share the same optical spectrum with the noise. The optimum electrical filter bandwidth for OOK was identified by Personick as 0.7 times the bit rate [51]. It should be noted that in our system thermal noise dominates. The receiver has a noise spectral density of 4.47 $pA/\sqrt{Hz}$ and 5 GHz bandwidth, which results in: $\sigma_{\mathrm{pre}}^2 = 0.1 \times 10^{-12}\mathrm{A}^2$; whereas for the red signal where the received power is 2.15×10^{-6} W, the shot noise is $\sigma_{\mathrm{shot}}^2 = 1.3819 \times 10^{-15}\mathrm{A}^2$. The

Table 1. Room configurations.

parameters	configurations			
room				
length × width × height	8 m × 4 m × 3 m			
walls and ceiling reflection coefficient	0.8 [48]			
floor reflection coefficient	0.3 [48]			
number of reflections	1	2		
area of reflection element	5 cm × 5 cm	20 cm × 20 cm		
order of lambertian pattern, walls, floor and ceiling	1 [48]			
semi-angle of reflection element at half-power	60°			
transmitters				
number of transmitters' units	8			
transmitters locations (x, y, z)	(1 m, 1 m, 3 m), (1 m, 3 m, 3 m), (1 m, 5 m, 3 m), (1 m, 7 m, 3 m), (3 m, 1 m, 3 m), (3 m, 3 m, 3 m), (3 m, 5 m, 3 m) and (3 m, 7 m, 3 m)			
number of RYGB LDs per unit	12			
transmitted optical power of red LD	0.8 W			
transmitted optical power of yellow LD	0.5 W			
transmitted optical power of green LD	0.3 W			
transmitted optical power of blue LD	0.3 W			
total transmitted power of RYGB LD	1.9 W			
semi-angle at half-power	60°			
Receiver				
number of photodetectors	4			
area of the photodetector	20 mm^2			
responsivity red	0.4 A W^{-1}			
responsivity yellow	0.35 A W^{-1}			
responsivity green	0.3 A W^{-1}			
responsivity blue	0.2 A W^{-1}			
photodetector	1	2	3	4
azimuth angles	45°	135°	225°	315°
elevation angles	70°	70°	70°	70°
field of view (FOV) of each detector	25°			
receiver noise current spectral density	4.47 pA/$\sqrt{}$Hz [49]			
receiver bandwidth	1.75 GHz			

SINR of user u, who is assigned wavelength λ of AP a, using branch f is, therefore, expressed as

$$\gamma_{u,f}^{a,\lambda} = \frac{\text{signal}}{\text{interference} + \text{noise}} = \frac{P_{u,f}^{a,\lambda} S_{u,f}^{a,\lambda}}{\sum_{\substack{b \in A \\ b \neq a}} \sum_{\substack{m \in U \\ m \neq u}} \sum_{g \in \mathcal{B}} P_{u,f}^{b,\lambda} S_{m,g}^{b,\lambda} + \sum_{\substack{b \in A \\ b \neq a}} \sigma_{u,f}^{b,\lambda} \left[1 - \sum_{\substack{m \in U \\ m \neq u}} \sum_{g \in \mathcal{B}} S_{m,g}^{b,\lambda} \right] + \sigma_{Rx}}, \tag{3.4}$$

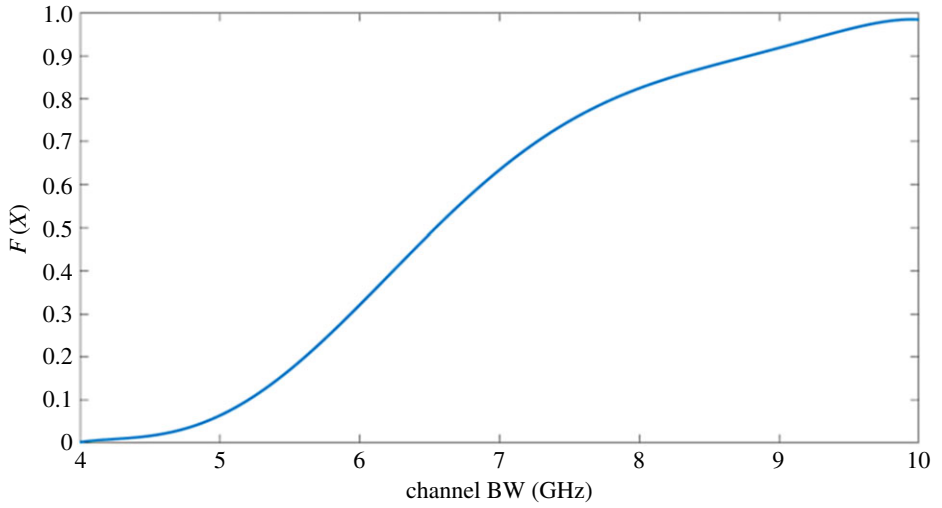

Figure 2. CDF of the optical channel bandwidth at different locations in the room using the parameters in table 1. (Online version in colour.)

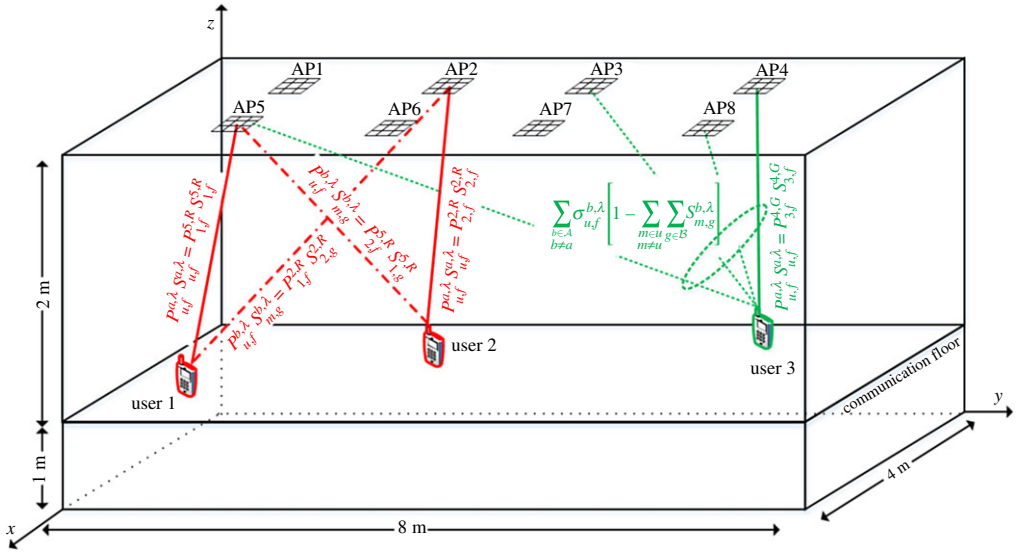

Figure 3. A room with three users. Solid lines indicate assignment of an access point to a user. Dot-dashed lines show interference between users using the same wavelength. Dotted lines indicate unmodulated wavelengths from access points causing background light shot noise. (Online version in colour.)

where $S_{u,f}^{a,\lambda}$ is a binary assignment variable that is equal to 1 if user u is assigned to AP a and wavelength λ and using branch f at the receiver. The first term in the denominator is the interference, which was calculated by summing the power received by user u from all APs where the same wavelength was used for communication, but assigned to other users, hence, causing interference. Furthermore, noise was calculated by summing two terms representing the receiver noise σ_{Rx} (calculated using equation (3.2)), which is constant for all users with identical receivers and background light shot noise. The background light shot noise $\sigma_{u,f}^{b,\lambda}$ is calculated using equation (3.3), which is the power received by the current user from all APs emitting unmodulated wavelengths identical to the current user's assigned wavelength (used for illumination only), hence causing shot noise. In other words, interference was calculated by summing the signal

powers of modulated light beams of the same wavelength, while background light shot noise was calculated by summing the signal powers of unmodulated wavelengths.

The interference term was calculated as the sum of the squared electrical currents and not by squaring the sum of the received optical powers multiplied by the responsivity of the photodetector. This simplifies the MILP implementation by maintaining linearity inside the MILP, while the squaring is carried out outside the MILP (pre-calculated). The error due to this method of calculation can be reduced by using the Cauchy–Schwarz inequality and introducing a factor n for the number of interferers, which can be either 0, 1 or 2 due to the tightened receiver's FOV. In the first two cases, there will be no error in the calculations. The error is only encountered when there are two interfering APs. Shot noise due to the interfering signal power was also ignored as it is much smaller than the preamplifier thermal noise and the background illumination-induced shot noise [52]. The maximization of the sum of SINRs on a linear scale, rather than throughput, which is a function of SINR as $B\log_2(1+\mathrm{SINR})$, simplifies the model, however, the introduction of the log function can help achieve two objectives. Firstly, the throughput or date rate is a more familiar metric than SINR, secondly, the log function will discourage the allocation of very high or very low SINR to individual users thus offering a form of fairness. The addition of a log function to calculate the throughput and add fairness is planned for the future.

Rewriting equation (3.4)

$$\sum_{\substack{b\in A\\ b\neq a}}\sum_{\substack{m\in U\\ m\neq u}}\sum_{g\in\mathcal{B}}\gamma_{u,f}^{a,\lambda}P_{u,f}^{b,\lambda}S_{m,g}^{b,\lambda}+\sum_{\substack{b\in A\\ b\neq a}}\gamma_{u,f}^{a,\lambda}\sigma_{u,f}^{b,\lambda}\left[1-\sum_{\substack{m\in U\\ m\neq u}}\sum_{g\in\mathcal{B}}S_{m,g}^{b,\lambda}\right]+\gamma_{u,f}^{a,\lambda}\sigma_{Rx}=P_{u,f}^{a,\lambda}S_{u,f}^{a,\lambda}\quad\forall u\in\mathcal{U},\forall a\in\mathcal{A},\forall\lambda\in\mathcal{W},\forall f\in\mathcal{B},\tag{3.5}$$

which can be rearranged as

$$\sum_{\substack{b\in A\\ b\neq a}}\sum_{\substack{m\in U\\ m\neq u}}\sum_{g\in\mathcal{B}}[P_{u,f}^{b,\lambda}-\sigma_{u,f}^{b,\lambda}]\gamma_{u,f}^{a,\lambda}S_{m,g}^{b,\lambda}+\sum_{\substack{b\in A\\ b\neq a}}\gamma_{u,f}^{a,\lambda}\sigma_{u,f}^{b,\lambda}+\gamma_{u,f}^{a,\lambda}\sigma_{Rx}=P_{u,f}^{a,\lambda}S_{u,f}^{a,\lambda}.\tag{3.6}$$

The first term containing the interference and background light shot noise from other APs is a nonlinear quadratic term involving the multiplication of a continuous variable by a binary variable. Linearization was performed following the same procedure in [53] as shown in equations (3.11)–(3.14) below.

The MILP model is defined as follows.

Objective: Maximize the sum of SINRs for all users,

$$\text{maximize}\sum_{a\in\mathcal{A}}\sum_{u\in\mathcal{U}}\sum_{\lambda\in\mathcal{W}}\sum_{f\in\mathcal{B}}\gamma_{u,f}^{a,\lambda}.\tag{3.7}$$

Subject to

$$\sum_{u\in\mathcal{U}}\sum_{f\in\mathcal{B}}S_{u,f}^{a,\lambda}\leq 1\quad\forall a\in\mathcal{A},\forall\lambda\in\mathcal{W}.\tag{3.8}$$

Constraint (3.8) ensures that a wavelength belonging to an AP is only allocated once, so, for all wavelengths and all APs, the assignment variables sum (over all users) to 0 if the resource is not allocated or 1 at maximum if the resource is allocated.

$$\sum_{a\in\mathcal{A}}\sum_{\lambda\in\mathcal{W}}\sum_{f\in\mathcal{B}}S_{u,f}^{a,\lambda}\geq 1\quad\forall u\in\mathcal{U}\tag{3.9}$$

and

$$\sum_{a\in\mathcal{A}}\sum_{\lambda\in\mathcal{W}}\sum_{f\in\mathcal{B}}S_{u,f}^{a,\lambda}\leq 1\quad\forall u\in\mathcal{U}.\tag{3.10}$$

Constraints (3.9) and (3.10) ensure that a user is assigned one wavelength. So, for all users, the sum of the assignment variable over all APs, wavelengths and branches is 1 (note that the result of using $\geq$ and $\leq$ in the two equations forces equality). These two constraints also ensure selection combining (SC) is used for the ADR receiver, i.e. only a single receiver branch is used per each user.

The following constraints (3.11)–(3.14) were used to linearize the multiplication process of the continuous variable by the binary variable in the quadratic term, where the non-negative linearization variable $\phi_{m,u,f}^{a,b,\lambda} = \gamma_{u,f}^{a,\lambda} S_{m,f}^{b,\lambda}$ is introduced:

$$\phi_{m,u,f}^{a,b,\lambda} \geq 0. \tag{3.11}$$

and

$$\phi_{m,u,f}^{a,b,\lambda} \leq \beta S_{m,f}^{b,\lambda} \quad \forall u, m \in \mathcal{U},\ \forall a, b \in \mathcal{A}, \forall \lambda \in \mathcal{W},\ \forall f \in \mathcal{B} \quad (u \neq \mathrm{m},\ a \neq b), \tag{3.12}$$

where β is a large number, so that $\beta \gg \gamma$.

$$\phi_{m,u,f}^{a,b,\lambda} \leq \gamma_{u,f}^{a,\lambda} \quad \forall u, m \in \mathcal{U},\ \forall a, b \in \mathcal{A}, \forall \lambda \in \mathcal{W},\ \forall f \in \mathcal{B} \quad (u \neq \mathrm{m}, a \neq b) \tag{3.13}$$

and

$$\phi_{m,u,f}^{a,b,\lambda} \geq \beta S_{m,f}^{b,\lambda} + \gamma_{u,f}^{a,\lambda} - \beta \quad \forall u, m \in \mathcal{U},\ \forall a, b \in \mathcal{A}, \forall \lambda \in \mathcal{W},\ \forall f \in \mathcal{B} \quad (u \neq \mathrm{m},\ a \neq b). \tag{3.14}$$

Using this linearization variable to replace the quadratic term, equation (3.6) can be rewritten as

$$\sum_{\substack{b \in A \\ b \neq a}} \sum_{\substack{m \in U \\ m \neq u}} \sum_{g \in \mathcal{B}} [P_{u,f}^{b,\lambda} - \sigma_{u,f}^{b,\lambda}] \phi_{m,u,f}^{a,b,\lambda} + \sum_{\substack{b \in A \\ b \neq a}} \gamma_{u,f}^{a,\lambda} \sigma_{u,f}^{b,\lambda} + \gamma_{u,f}^{a,\lambda} N_0 = P_{u,f}^{a,\lambda} S_{u,f}^{a,\lambda}. \tag{3.15}$$

In order to support a BER of 10^{-9} using OOK modulation (our chosen modulation format here), the SINR should not go below 15.6 dB. The same performance (BER of 10^{-9}) can, however, be achieved with a lower SINR using forward error correction techniques at the expense of an increased data rate overhead[1]. Here, 10% overhead is assumed (worst case) when SINR decreases to 12 dB. This is added as a constraint

$$\gamma_{u,f}^{a,\lambda} \geq 10^{12/10} \quad \forall u \in \mathcal{U},\ \forall a \in \mathcal{A}, \forall \lambda \in \mathcal{W}, \forall f \in \mathcal{B}. \tag{3.16}$$

The MILP model was solved using the CPLEX solver over the University of Leeds high-performance computer (Polaris) using 16 nodes (256 cores) with 16 GByte of RAM per core. Each node comprises two eight-cores of the Intel 2.6 GHz Sandy Bridge E5-2670 processors. CPLEX 12.5.0.0 was used with around 194 mixed-integer programming (MIP) simplex iterations for the first scenario, while 159 MIP simplex iterations were used for the second scenario and 92 MIP simplex iterations were used for the third scenario. The computational requirements thus changed for different scenarios. This is an NP hard problem. After the assignment of APs and wavelengths was optimized using the MILP model, the optical channel bandwidth, the SINR and achievable data rates were calculated for each user and scenario (table 2) in this study, and they are shown in figures 4–6.

It should be noted that the supported data rate can be limited by one of three factors: the modulation bandwidth of the light source, the optical channel bandwidth or the receiver bandwidth. Since LDs were used in this study, they do not limit the data rate as they can support modulation rates at GHz rates beyond those in our study [49]. To address the second limiting factor, the use of ADR improves the optical channel bandwidth as it limits the number of incident rays from different reflecting elements, hence, the delay spread is reduced and the channel bandwidth increases. From equation (3.2), it can be seen that the receiver bandwidth can be used to control the amount of shot noise attributed to light sources as reducing the optical bandwidth

[1]For more information refer to http://www.ieee802.org/3/10G_study/public/july99/azadet_1_0799.pdf where, for example, it is stated that "RS(255 239) overhead is 6% for input BER = 10^{-4}, output BER = 10^{-14}".

Table 2. The scenarios considered and the resulting optimized allocation of APs and wavelengths.

	scenario 1				scenario 2				scenario 3			
user	location (*x*,*y*,*z*)	AP	receiver branch	wavelength	location (*x*,*y*,*z*)	AP	receiver branch	wavelength	location (*x*,*y*,*z*)	AP	receiver branch	wavelength
1	(0.25,0.25,1)	1	1	blue	(0.5,6.5,1)	3	4	red	(0.5,5.5,1)	3	4	red
2	(0.25,0.75,1)	1	1	green	(0.5,7.5,1)	4	4	yellow	(1.5,1.5,1)	1	3	red
3	(0.75,0.25,1)	1	1	yellow	(1.5,6.5,1)	8	1	red	(1.5,3.5,1)	2	3	red
4	(0.75,0.75,1)	1	1	red	(1.5,7.5,1)	4	3	red	(1.5,7.5,1)	4	3	red
5	(3.25,7.25,1)	8	3	red	(2.5,0.5,1)	5	1	red	(2.5,2.5,1)	6	1	red
6	(3.25,7.75,1)	8	3	yellow	(2.5,1.5,1)	1	3	red	(2.5,6.5,1)	8	1	red
7	(3.75,7.25,1)	8	3	green	(3.5,0.5,1)	5	2	yellow	(3.5,1.5,1)	5	3	red
8	(3.75,7.75,1)	8	3	blue	(3.5,1.5,1)	6	2	red	(3.5,4.5,1)	7	2	red

royalsocietypublishing.org/journal/rsta *Phil. Trans. R. Soc. A* **378**: 20190188

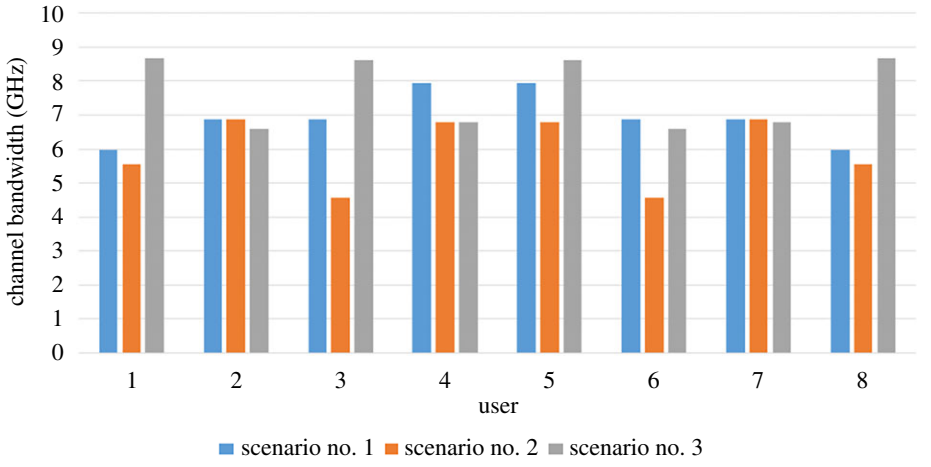

Figure 4. Optical channel bandwidth. (Online version in colour.)

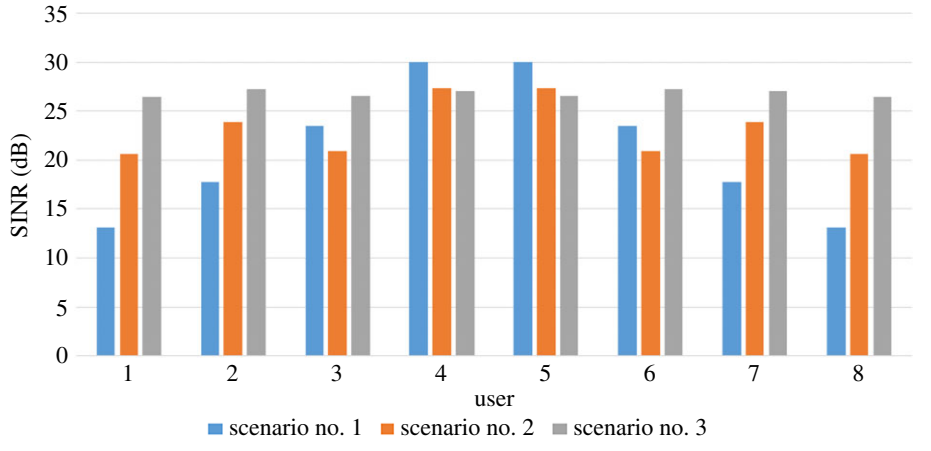

Figure 5. SINR for different users. (Online version in colour.)

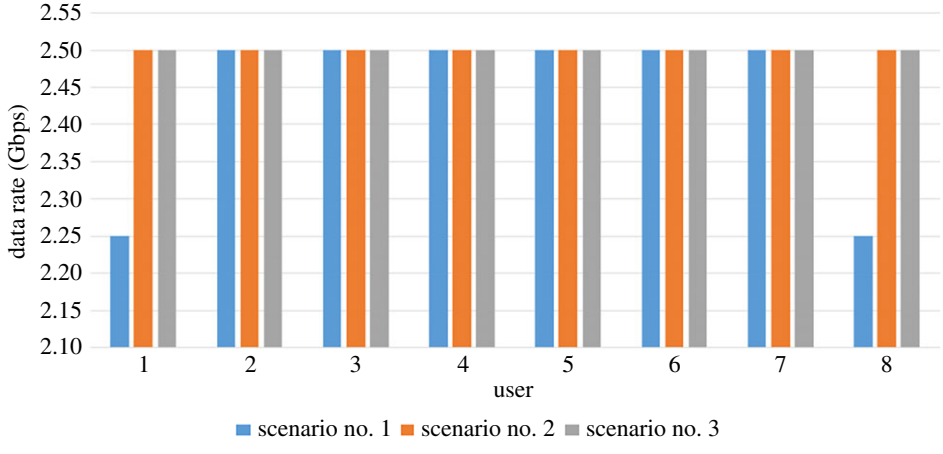

Figure 6. Data rates for different users. (Online version in colour.)

will affect the signal too as it shares the same optical spectrum as the noise. Also, from equation (3.3), the preamplifier noise can be reduced by reducing the receiver bandwidth. Reducing the electrical filter bandwidth will, however, lead to increased ISI. The optimum bandwidth of the electrical filter, for OOK, was identified as 0.7 times the bit rate [51]. The SINR is also affected by interference, which increases when the number of users sharing the same wavelength increases in WDM as well as when the amount of overlap between the coverage area of different APs increases. Since VLC is used, the same shade of white light generated using RYGB LDs by the authors of [30] is assumed in this study, i.e. only four wavelengths are assumed; and VLC requires large coverage area per AP to meet the illumination standards. A combiner is used to combine the four laser beams then a hologram/diffuser is used in front of the LDs to spread the radiation angle of the LD and destroy its spatial coherence. This allows the tailoring of the radiation pattern and achieves a wide half-power semi-angle [30,49]. Thus each AP had a half-power semi-angle of 60° in our system. The VLC system performance can however be improved by optimizing the allocation of APs and wavelength resources to minimize interference so that the overall sum SINR is maximized.

Three realizations (scenarios) are selected (where users' coordinates are clustered under an AP or spread over the room) for which the optimization was performed based on the best detector of the ADR for each user location. Statistical distribution of users will be treated in future work using stochastic optimization.

After optimizing the allocation of each user to an AP and a wavelength (table 2), the optical bandwidth, the SINR and data rates, were calculated based on selecting the best detector of the ADR for each user location and shown in figures 4–6, respectively.

The channel bandwidth is calculated from the channel impulse response for each combination of transmitter and receiver location and this shows a minimum bandwidth of around 4.5 GHz and a maximum bandwidth of 8.7 GHz for the users in the three scenarios (based on tables 1 and 2). This calculation is independent of the colour used. The SINR was calculated based on the results of the optimized allocation of an AP and a wavelength to each user using the best receiver branch, where the noise and the interference are calculated based on the resources allocated (as shown in figure 3). The results show a minimum SINR of around 12 dB for the users in the three scenarios where the use of the receiver in table 1 is assumed. The calculated values of data rates for different users are used in the next section where a MILP model is developed to optimize the placement of the processing in the integrated cloud/fog with OWC system to minimize the overall power consumption.

4. Optimum placement of processing to minimize power consumption

The proposed integrated cloud/fog architecture is shown in figure 7, which builds on our work in the optimization of distributed data centres [54–57], network architecture optimization [58–62] and energy-efficient routing [63–67]. It consists of one or more OW mobile users in a room clustered as a mobile fog unit (MobFog). Each mobile device communicates with one or more light units (APs) and is assigned to one of the channel wavelengths, red, yellow, green or blue (RYGB). All APs are connected to a passive optical network, where each AP is also connected to an optical network unit (ONU). All ONUs are connected to a central OLT located in the same room. The room is also equipped with a commodity server (low-end computer), which acts as a mini fog node (RoomFog). This node is connected to the central OLT through an ONU and an optical link. The proposed architecture introduces three more fog data centres located in the building (BuildFog), campus (CampFog) and metro network layer (MetroFog). This architecture is integrated with the central cloud data centre (CCloud) through an optical infrastructure to support high demand requests that cannot be fulfilled by mobile units or fog nodes.

The OLT acts as a controller unit [68] that collects processing requests from mobile units present in the same room. These requests can be generated from applications in the mobile units. The mobile units transmit the data to be processed. The knowledge extracted after processing

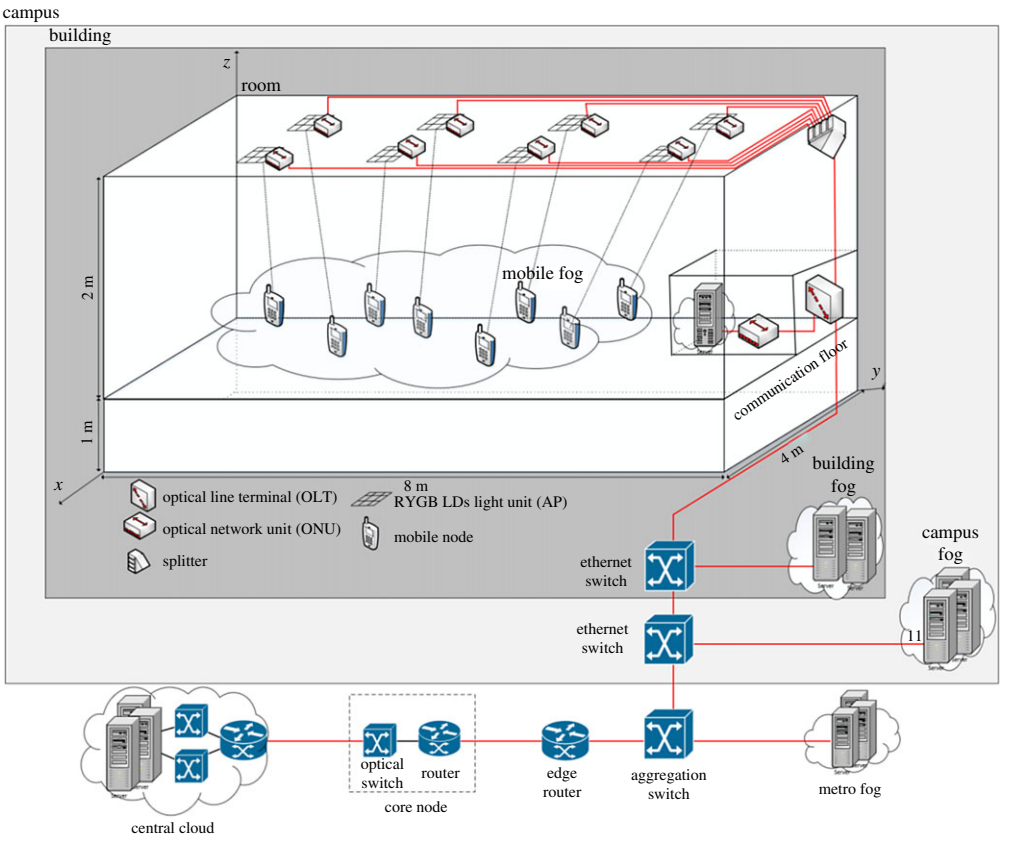

Figure 7. Cloud/fog-based architecture. (Online version in colour.)

the data (for example, (i) the presence or absence or someone in a transmitted video sequence; or (ii) whether a person is fine or not after transmitting a large heart rate signal) is always smaller than the transmitted data [69–71]. The OLT also assigns in an optimal way (MILP in this section) the collected requests to the Central Cloud or any fog node to be processed. When the OLT decides that a task / demand is to be processed by the MobFog, it allocates this task to the participants' mobiles through VLC communication and then forwards the processing results back to the OLT. If the OLT decides to assign the demand to the RoomFog, BuildFog or CampFog nodes, the demand will be sent through a local Ethernet LAN to the required location. For the MetroFog and CCloud assignment, demands traverse through the optical infrastructure to either location. The tasks allocation was optimized using a MILP model to minimize the power consumption of the overall architecture while considering different OW data rates depending on the scenario. Below are the notation of the parameters and the variables used in this optimization model.

In this MILP model, the sets are defined as follows:

N	set of all nodes;
Nm_i	set of nodes that are neighbours of node i;
PN	set of processing nodes;
SN	set of source nodes;
K	set of tasks (demands).

The following parameters are also defined:

W_{ks}	workload demand of task k generated from source node s, in million instructions per second (MIPS);
F_{ks}	flow (data rate) demand of task k generated from source node s (in Mbps);
C_n	workload capacity of processing node n (in MIPS);
L_{ij}	capacity of the link between nodes i and j (in Mbps);
E_n	power per MIPS of processing node n (W/MIPS);
Ψ_n	power per Mbps of the route to the processing node n (W/Mbps).

The following variables are also defined:

P_n	total power consumption due to data processing;
$\mathcal{P}_n$	total power consumption due to networking;
X_{kn}	task k processing workload, in MIPS, assigned to processing node n;
δ_{kn}	binary variable, $\delta_{kn} = 1$ if task k is assigned to processing node n, 0 otherwise;
L_{ksd}	traffic flow of task k sent from source node s to processing node d;
λ_{ij}^{ksd}	traffic flow of task k sent from source node s to destination (processing node) d through physical link i and j.

The model's objective is to minimize the power consumption of the overall proposed architecture, including the processing and networking power consumption of the processing locations, and the network connecting these locations, as presented below in equation (4.1).

Objective: Minimize

$$\sum_{n \epsilon PN} P_n + \sum_{n \epsilon PN} \mathcal{P}_n. \tag{4.1}$$

The objective equation consists of two terms: the power consumed by processors due to computation and the power consumed by transmitting traffic through the network. Note that in our network topology, in figure 7, there is a single route between the OW mobile units and each processing node option (CCloud, MetroFog, CampFog, BuildFog, RoomFog or other mobile units in the MobFog).

The power consumption of this route is given by one value as explained in equation (4.3). Therefore, the second term in equation (4.1) is summed over processing nodes (as there is a single network path to each processing node in our case).

The processing power consumption, P_n is given as

$$P_n = \sum_{k \epsilon K} X_{kn} E_n \quad \forall n \in PN, \tag{4.2}$$

where X_{kn} is the workload demanded by task k, in million instructions per second (MIPS), assigned to processing node n. E_n is the energy in watts per MIPS of the node processor, calculated using the maximum processing capacity of the node.

The networking power consumption, $\mathcal{P}_n$ is given as

$$\mathcal{P}_n = \sum_{k \epsilon K} \delta_{kn} F_{ks} \Psi_n \quad \forall n \in PN, s \in SN, \tag{4.3}$$

where δ_{kn} is a binary variable which specifies the allocation of task k to processing node n, and F_{ks} is the task data rate demand (in Mbps) generated from source node s. Ψ_n is the total power per Mbps of all nodes between the source and the assigned processing node (in Watts per Mbps). For the OW link, the power per Mbps value is calculated based on the individual wavelength colour (RYGB) used for the connection.

The model is subject to the following constraints:

Processing allocation constraints

$$\alpha X_{kn} \geq \delta_{kn} \quad \forall k \in K, n \in PN \tag{4.4}$$

and

$$X_{kn} \leq \alpha \delta_{kn} \quad \forall k \in K, n \in PN, \tag{4.5}$$

Constraints (4.4) and (4.5) ensure that task k is assigned to processing node n.

$$\sum_{n \epsilon PN} \delta_{kn} = 1 \quad \forall k \in K. \tag{4.6}$$

Constraint (4.6) ensures that each task k will be assigned to one processing node.

Processing node capacity constraint

$$\sum_{k \epsilon K} X_{kn} \leq C_n \quad \forall n \in PN. \tag{4.7}$$

Constraint (4.7) ensures that each task k assigned to a processing node n does not exceed the processing capacity of this processing node.

Link capacity constraint

$$\sum_{k \epsilon K} \sum_{\substack{s \epsilon SN \\ d \epsilon PN}} \lambda_{ij}^{ksd} \leq L_{ij} \quad \forall i \in N, j \in Nm_i, i \neq j. \tag{4.8}$$

Constraint (4.8) ensures that the traffic of task k sent from source s to processing node d does not exceed the capacity of the link between any two nodes i and j.

Flow conservation constraint

$$\sum_{\substack{j \in Nmi \\ i \neq j}} \lambda_{ij}^{ksd} - \sum_{\substack{j \in Nmi \\ i \neq j}} \lambda_{ji}^{ksd} = \begin{cases} L_{ksd} & if\ i = s \\ -L_{ksd} & if\ i = d \\ 0 & \text{otherwise} \end{cases} \quad \forall k \in K, s \in SN, d \in PN, i, j \in N. \tag{4.9}$$

Constraint (4.9) ensures that the total incoming traffic is equal to the total outgoing traffic for all nodes except for the source and destination nodes.

$$L_{ksd} = F_{ks} \delta_{kd} \quad \forall k \in K, s \in SN, d \in PN. \tag{4.10}$$

Constraint (4.10) ensures that the traffic from source node s to destination node d is equal to the data rate of task k generated from source s. δ_{kd} is a binary variable used to ensure that task k is assigned to destination d.

The main outputs of the MILP model in this section are the values of the δ_{kd} decision variable. Therefore, this is an optimal placement and routing problem and solution. Based on the value of δ_{kd}, the networking and processing power consumption splits can be determined.

The flow process of any generated request follows six phases. Firstly, a request is generated by a mobile unit and sent to the OLT, which has full knowledge of the available resources. Secondly, the OLT sends a positive acknowledgement to the source node. These two phases are not considered in the model as they generate negligible traffic. Thirdly, the data to be processed are sent in an uplink from the mobile source node to the OLT through the OW channel. This phase is also not considered in the model as it is a common phase for all requests and will not affect the placement decision. Fourthly, the data to be processed are offloaded from the OLT to one of the available processing nodes (MobFog, RoomFog, CampFog, BuildFog, MetroFog or CCloud). As this phase carries the main data, this will affect the power consumption and the placement decision. Therefore, it is treated as the main component of the model. Note that processing the task locally in the mobile unit that has requested this service is not an option for the assumed scenarios. In the last two phases, the extracted knowledge resulting from the processed data is

Table 3. Processing node capacities and power efficiencies.

processing node (server)	power consumption (W)	capacity (MIPS)	efficiency (W/MIPS)	route efficiency (W/Mbps)
Central Cloud (Intel® Xeon® E5-2680)	115 [72]	144 000 [72]	0.000799	0.128
MetroFog (Intel X5675)	95 [73]	73 440 [73]	0.00129	0.0713
CampFog (Intel Core2-Q9400)	95 [74]	35 160 [74]	0.0027	0.0475
BuildFog (Intel Xeon E5-2420)	95 [75]	34 200 [75]	0.0028	0.0238
RoomFog (Intel Core i7-6500U)	15 [76]	5000 [76]	0.003	0.0015
Mobile unit (HTC One X)	6.66 [77]	1500 [77]	0.0044	0.00222 (red)
				0.00195 (yellow)
				0.00177 (green)
				0.00177 (blue)

sent back from the processing node to the OLT, and so to the source mobile unit that requested the service. As we assume that the extracted knowledge has a small volume compared with the main data, the last two phases are not considered in the optimization model.

In order to highlight the effect of the new integration between fog processing and OW communication, the task allocation optimization model has been evaluated here using an ideal scenario with eight mobile units located in the room. Each mobile unit is connected to a single light unit (AP) through one of the wavelengths (RYGB). Note that the sum of the OWC link capacities is restricted by the maximum capacity of the ONU connected to the AP, which is equal to 10 Gbps. This ideal scenario is compared at the end with the three scenarios resulting from the resource allocation model in §3.

We have evaluated the power consumption in the above-mentioned scenarios for an architecture composed of different fog servers in each layer. Based on the servers considered, the processing energy of the CCloud server is 82% more efficient than that of a mobile processor, followed by MetroFog, CampFog, BuildFog and then the RoomFog server, which has just 32% of the processing energy efficiency of a mobile processor. On the other hand, because of the location of the CCloud and other fogs, the networking power consumption when traffic is sent to the RoomFog, is 98% lower than with the CCloud. This is because the RoomFog server is only one hop away from the OLT controller, from which the tasks are offloaded. This networking energy increases by 1–3 mW $Mbps^{-1}$ when the tasks are offloaded to the MobFog, based on the wavelength assigned to each mobile unit.

Table 3 summarizes the capacity, power consumption and energy efficiency values of the processing nodes and the energy efficiency values of each route leading to each node, while table 4 provides the maximum capacity, power consumption and efficiency values for each individual networking device. The energy efficiency of a processing/networking node is calculated as explained in equation (4.11). Note that there is a single server in each of the five cloud and fog-processing locations in table 3. Therefore, the values of the networking energy efficiencies for different routes are defined there for each processing location. The energy efficiency in Joules per bit for a path is the sum of all networking devices energy efficiency values between the controller and the processing node (excluding the OLT energy efficiency value as it is common to all routes).

$$\text{node energy efficiency} = \frac{\text{maximum power consumption}}{\text{maximum capacity}}. \tag{4.11}$$

The MILP model was evaluated to show the effects of the proposed architecture on the power consumption. We also studied the effects of different OW wavelengths on the processing utilization of the mobile units assigned. In this evaluation, 50 tasks were considered, with workload processing demands ranging between 100 and 1500 MIPS. In equation (4.12), we

Table 4. Network device capacities and power efficiencies.

network device	power consumption	capacity (Gbps)	device efficiency (W/Mbps)
OLT (Tellabs1134)	400 W [78]	320 [78]	0.00125
ONU (FTE7502 10G)	15 W [79]	10 [79]	0.0015
central cloud switch (cisco 6509)	3.8 kW [80]	320 [80]	0.012
central cloud router (Juniper MX-960)	5.1 kW [80]	660 [80]	0.008
core router (Cisco CRS-1 16-slots)	13.2 kW [81]	1200 [81]	0.011
transponder (in core node) (ONS15454)	50 W [82]	10 [82]	0.005
optical switch (Cisco SG220)	63.2 W [83]	100 [83]	0.0006
edge router (Cisco 12816)	4.2 kW [84]	200 [84]	0.021
aggregation switch (Cisco 6880)	3.8 kW [85]	160 [85]	0.024
ethernet switch (Cisco 6880)	3.8 kW [85]	160 [85]	0.024
access point (using red wavelength)	7.2 W	10	0.00072
access point (using yellow wavelength)	4.5 W	10	0.00045
access point (using green wavelength)	2.7 W	10	0.00027
access point (using blue wavelength)	2.7 W	10	0.00027

introduce the relation between the workload demand and the data rate demand for each requested task as a ratio, termed the 'data rate ratio' (DRR). Different DRR values were defined in the model, varying between 0.002 and 0.6 to consider different scenarios with low and high data rates.

$$\text{data rate demand} = \text{DRR} \times \text{workload demand}. \tag{4.12}$$

The goal is to examine the impact of increase in the demand values interpreted in terms of increase in the processing workload and data rate. We assumed that the data rate of any task increases with increase in the processing workload. Therefore, we introduced the DRR parameter to capture different ratios between these two values (processing workload and data rate) and to cover a wide range of demand values. The following are the values considered for DRR: 0.002, 0.02, 0.04, 0.06, 0.2, 0.4 and 0.6. As examples of the type of applications represented by these DRR values, a DRR value of 0.002 represents a task that is intensive in processing and light in communication, for example sensing simple data and then processing it intensively. At the other extreme DRR = 0.6 may represent video gaming that is intensive in communication and processing. Other applications may include processing video, images or large sensor files.

The results are first presented for the ideal scenario, in which each mobile unit is connected to a single light unit with full, 10-Gbps data rate capacity through one of the wavelengths (RYGB). Then results are given for scenarios 1, 2 and 3, in which the eight users are assigned different wavelengths with varied data rates, based on their location. The different data rate values for each user in both of these scenarios are extracted from those given in figure 6.

The results in figure 8 show the processing power consumption, the networking power consumption and the overall power consumption versus the processing workload per demand for different DRR values.

The processing power consumption shown in figure 8*a* indicates that at low DRR, the data rate is minimal and the networking power consumption becomes negligible. Hence, the location with the best processing energy efficiency is selected (the central cloud in DRR = 0.002 and MetroFog in DRR = 0.02). On the other hand, processing power consumption in DRR = 0.04 and 0.06 starts linearly up to a certain workload demand (800 MIPS), as in figure 8*a*. After this point, a clear increase in the power consumption occurs when the most efficient locations, in total power

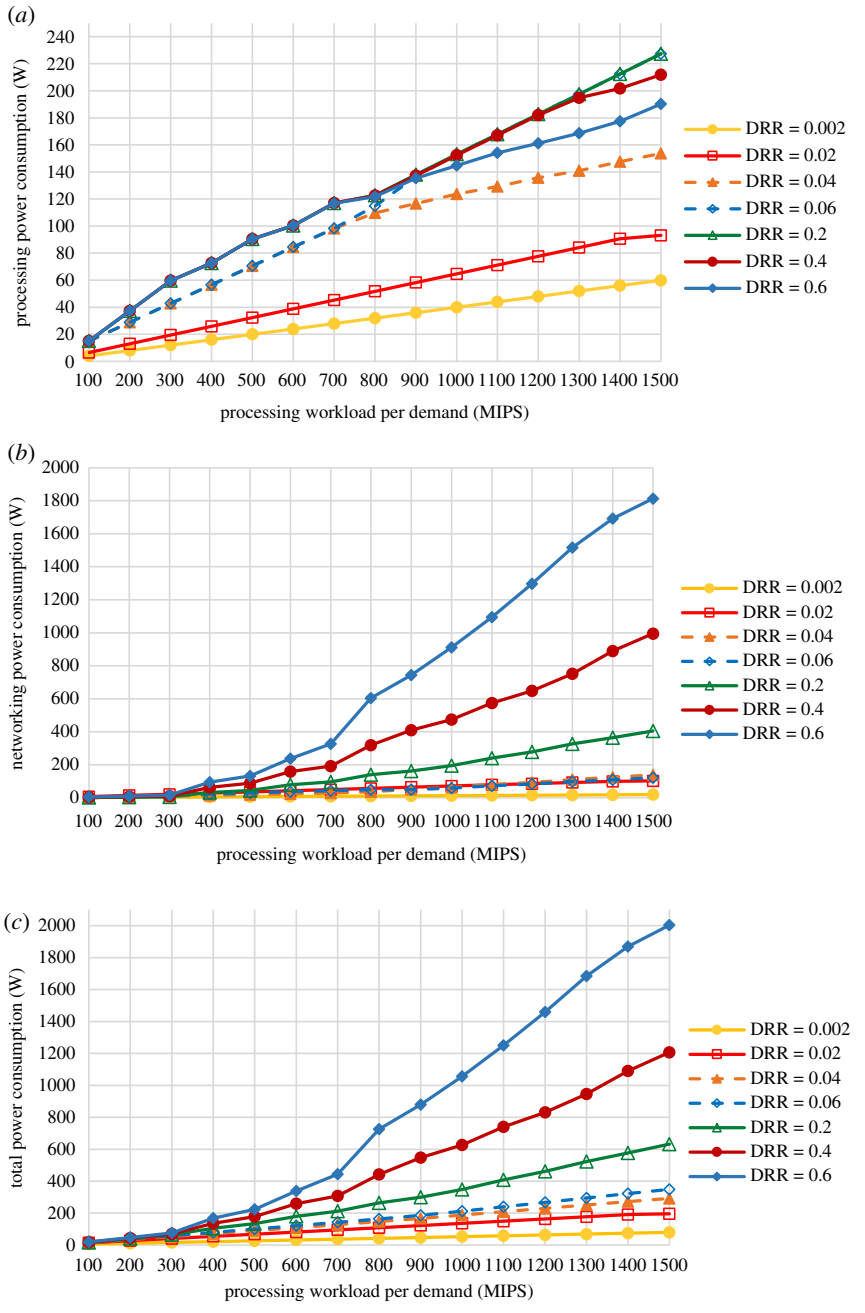

Figure 8. Processing, networking and total power consumption versus processing workload per demand, for different DRR values. (*a*) Processing power consumption, (*b*) networking power consumption and (*c*) total power consumption. (Online version in colour.)

consumption, start to become exhausted and the workload is consequently offloaded to other processing locations. It is also worth mentioning that in the case of DRR = 0.04, the RoomFog becomes more efficient in processing the workload, followed by BuildFog and then MetroFog. At DRR = 0.06, however, the MobFog performs better in terms of energy efficiency than MetroFog due to its efficient networking energy. At higher DRRs, the processing power consumption of the MobFog increases (between 100 and 800 MIPS with DRR = 0.2, 0.4 and 0.6).

The increase varies according to the different workload demands assigned. For instance, with 300 MIPS, each mobile node can process five tasks with a total possible allocation of 1500 MIPS assigned to the mobile unit. This causes an increase in the processing power consumption, as the mobile units are the least efficient processors.

On the other hand, with 400 MIPS demand, three tasks assigned to each mobile unit have a total of 1200 MIPS allocation, which causes a reduced processing power consumption compared with the 300 MIPS case. These variable allocations are due to the limited capacity of the mobile unit and the single allocation constraint. Also, at the highest two DRR values, 0.4 and 0.6, the BuildFog and CampFog communication links become the bottleneck. Thus, processing is placed further out in the MetroFog, which reduces processing power consumption.

Figure 8*b* reveals the higher impact of the networking power consumption with increase in the workload demands at high DRR values. This affects the total power consumption as seen in figure 8*c*, which becomes highly related to the networking power consumption. Figure 8*b* shows that as DRR increases, i.e. as the communication data rate increases, the networking power consumption increases. At low DRR (0.002 and 0.02), the networking power consumption values are comparable and increase linearly with a very low power consumption. This is because the networking power consumption for such low rates becomes negligible with a minimum effect on the allocation decision. Consequently, the workload demands in these two cases are placed in one location (the location with the best processing efficiency).

At DRR = 0.04 and 0.06, the placement decision remains affected by the processing power consumption. This results in a small increase at DRR = 0.04 compared with that at 0.06 because the workload is offloaded to a further location (MetroFog) at 0.04 while at 0.06 it is offloaded to a more networking-efficient location (CampFog). A meaningful increase is shown at higher data rates, with DRR = 0.2, 0.4 and 0.6. This power increases more significantly after a certain point (750 MIPS), when the mobile unit processor cannot process more than one task due to its limited capacity (1500 MIPS). In this case, more demands are offloaded to the CampFog, which increases the networking power consumption. It is notable that at DRR = 0.2, the power consumption has a slow increase as the tasks are assigned to the most efficient destination in terms of networking power consumption. By contrast, the power consumption increases more at DRR = 0.4 and 0.6. The first reason for this is the limitation of the network links of BuildFog and CampFog, which cannot support very high traffic (in excess of 10 Gbps). Consequently, more tasks are offloaded to locations with lower networking energy efficiency. The second reason is the limited processing capacity of the mobile, which results in the offloading of more demands further out.

Figure 9 shows the overall workload allocation for each processing location in relation to the networking power consumption for the case of DRR = 0.6. For the assigned workload, the figure shows where demands are placed for each given data rate and how this affects the networking power consumption of this placement. Starting from low data rate demands, demands are assigned to the most efficient location in term of total power consumption (RoomFog followed by MobFog, BuildFog, CampFog and then MetroFog). Note that CCloud is not assigned any workload to satisfy the demand caused by any closed fog locations. Also, the networking power consumption for low data rate demands is very low due to the demands placed at RoomFog and MobFog. This power consumption is dominated by other fogs which are less efficient networking locations; thus, the networking power consumption becomes significant. More details about the networking power consumption splits for each DRR are shown in figure 10.

As mentioned above, this ideal scenario considers a constant data rate wavelength assigned to each mobile unit. For scenarios 1, 2 and 3, the data rate is limited based on the user location and number of users accessing the same AP, as explained (in the previous section) and summarized in table 5. Figure 11 shows the processing, networking and total power consumption for these three scenarios, compared with the ideal scenario and with a baseline scenario where processing is always carried out at the central cloud. The conventional (baseline) case consumes the highest power as all demands are placed at the central cloud and therefore consume the highest networking power consumption, which affects the total power. The other three scenarios (1, 2 and 3) have very comparable results with the ideal scenario. This indicates that the demands

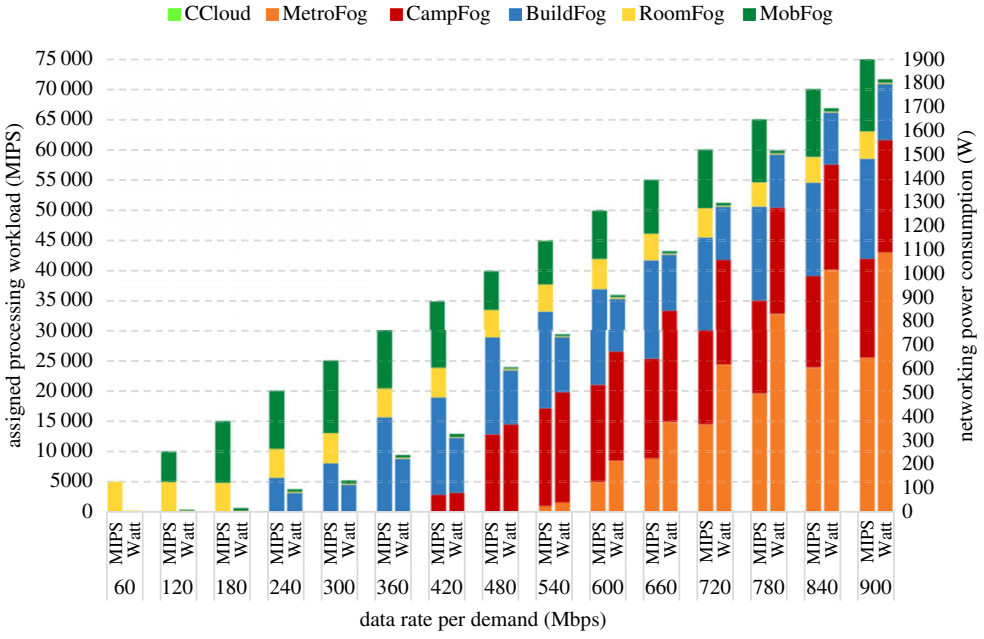

Figure 9. Assigned processing workload and networking power consumption versus data rate per demand, for each cloud and fog node (DRR = 0.6). (Online version in colour.)

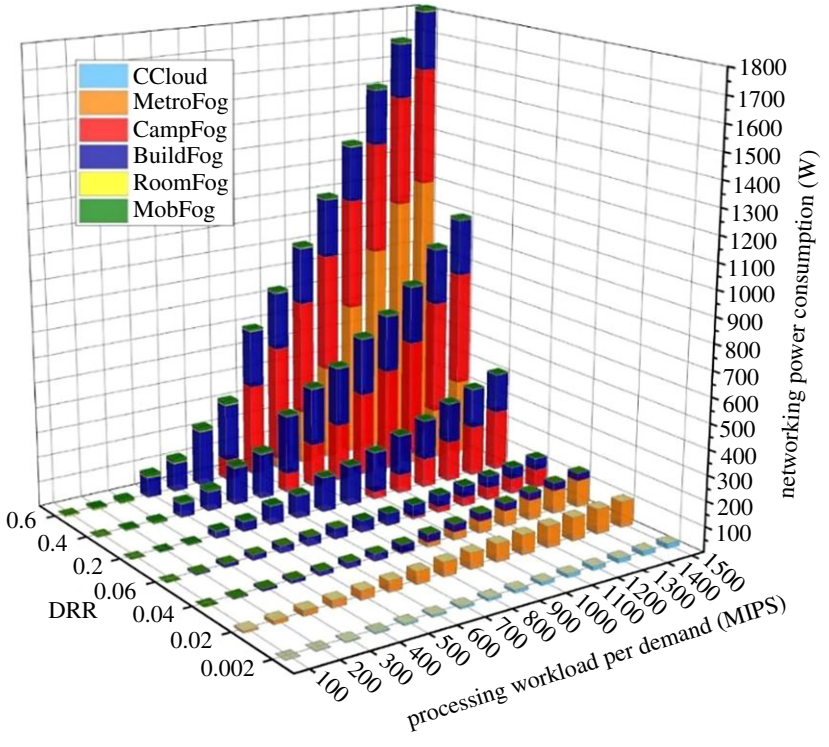

Figure 10. Networking power consumption versus workload per demand and DRR value, for each cloud and fog node. (Online version in colour.)

Table 5. Wavelength efficiency values for scenario 1, scenario 2 and scenario 3.

	scenario 1			scenario 2			scenario 3		
wavelength	maximum capacity (Gbps)	maximum power (w)	efficiency (W/Mbps)	maximum capacity (Mbps)	maximum power (w)	efficiency (W/Mbps)	maximum capacity (Mbps)	maximum power (w)	efficiency (W/Mbps)
red	2.50	7.2	0.0044	2.50	7.2	0.004	2.50	7.2	0.004
yellow	2.50	4.5	0.0033	2.50	4.5	0.003	0	4.5	N/A
green	2.50	2.7	0.0026	0	2.7	N/A	0	2.7	N/A
blue	2.25	2.7	0.0027	0	2.7	N/A	0	2.7	N/A

royalsocietypublishing.org/journal/rsta *Phil. Trans. R. Soc. A* **378**: 20190188

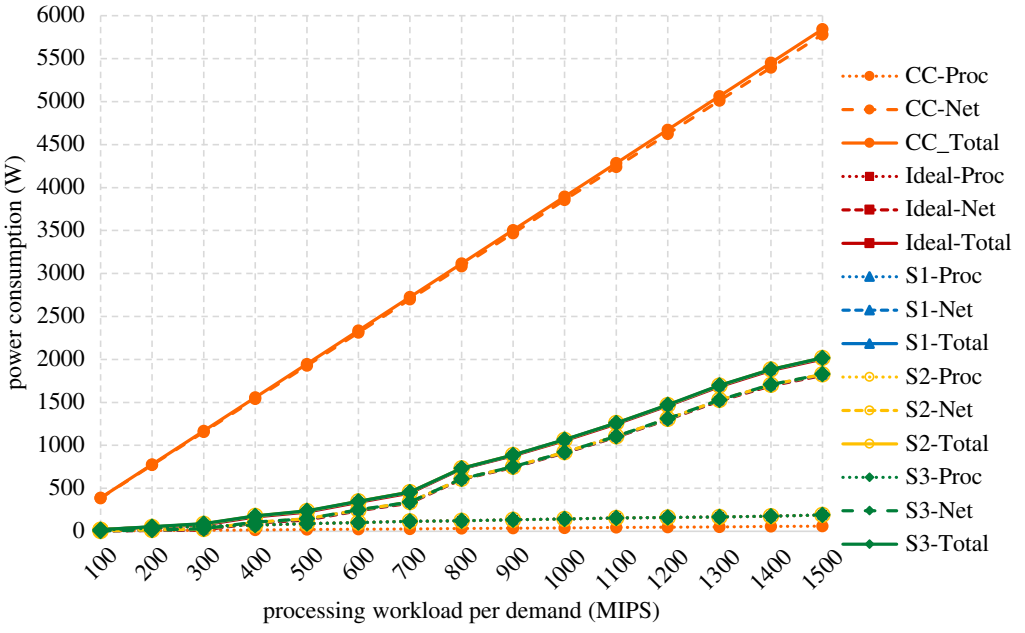

Figure 11. Processing power consumption, networking power consumption and total power consumption, for conventional cloud scenario (CC), ideal scenario (ideal), scenario 1 (S1), scenario 2 (S2) and scenario 3 (S3) with DRR = 0.6. (Online version in colour.)

allocation and therefore the consumed power are not affected by the different assigned channel data rates if these channels satisfy the networking demand and the mobile units satisfy the workload demand. However, compared with the central cloud scenario, scenarios 1, 2 and 3 save power by an average of 79% compared with the central cloud allocation.

Figure 12 shows the mobile units processing utilization based on the assigned wavelength for the four scenarios (ideal, 1, 2 and 3). In scenario 1, each user is assigned a channel with data rate capacity ranging from 2.25 to 2.50 Gbps, while users are assigned channels equal to 2.50 Gbps in scenario 2 and 3. Based on the new capacity values for each link, the wavelength power efficiency is affected as explained in table 5.

Figure 12*a* shows that, in the ideal scenario, the mobile unit utilization is equal to zero at the lowest data rate demands as all the workload demands are assigned to the RoomFog. At 120 Mbps, the processors of mobile units assigned to blue and green wavelengths are occupied first as these have the lowest wavelength energy requirements (table 3). At 180 Mbps, mobile units assigned blue, green and yellow wavelengths achieved their full utilization, followed by mobile units assigned to the red wavelength, which has the highest energy usage. At 240 Mbps, all mobile units achieved only 80% utilization due to bin packing and single allocation considerations. For instance, based on the DRR value (0.6), the workload demand at 240 Mbps is equal to 400 MIPS for all 50 tasks. With a mobile processor capacity equal to 1500 MIPS, each mobile unit can serve three tasks with a maximum allocation of 1200 MIPS per unit. However, full utilization is achieved at 300 Mbps as three tasks are assigned to each mobile unit with a total allocation that is equal to the mobile processing capacity. At 360 Mbps, the utilization decreased to 80%, due to the same bin packing and single allocation considerations. This utilization increases to 93% at 420 Mbps as the demand workload is equal to 700 MIPS so each mobile unit is assigned two tasks with a total allocation of 1400 MIPS per unit. A significant utilization drop occurs afterwards, at 480 Mbps, as the workload per demand increases to 800 MIPS. This is due to the limited processing capability of the mobile unit, which cannot serve more than one task, causing the mobile processor to achieve only 53% utilization. The constant increase in the workload demand causes a constant increase

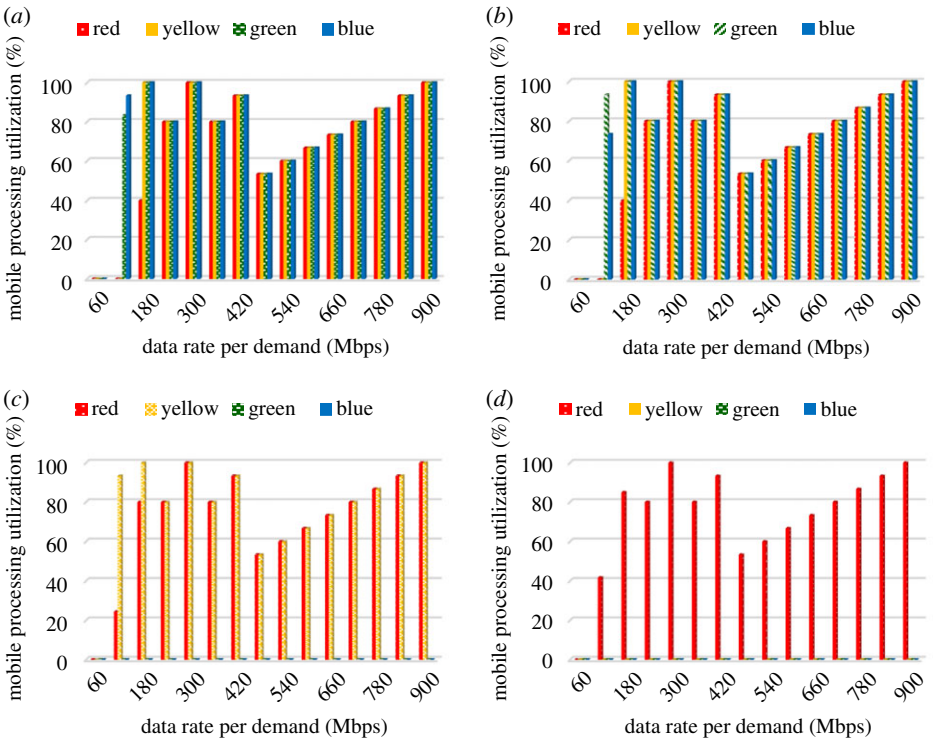

Figure 12. Mobile processing utilization per assigned wavelength for the ideal scenario, scenario 1 (S1), scenario 2 (S2) and scenario 3 (S3) with DRR = 0.6. (*a*) Mobile processing utilization in the ideal scenario, (*b*) mobile processing utilization in scenario 1, (*c*) mobile processing utilization in scenario 2, (*d*) mobile processing utilization in scenario 3. (Online version in colour.)

in the mobile unit utilization, which ranges between 60% (at 540 Mbps), and 100% (at the highest considered workload demand, 1500 MIPS).

The task allocation behaviour with the increase in demands in the other three scenarios in figure 12*b–d* follows the same behaviours described in figure 12*a* taking into account the fact that the varied link capacity and updated wavelength efficiencies affect the task allocation decision. For example, in scenario 1 in figure 12*b*, the power efficiency of the green wavelength has the best values, followed by blue, yellow, and finally red wavelength. This is reflected in the assignment decision and therefore giving the mobile units allocated a green wavelength priority when it comes to the processing allocation. The same observation is seen in scenario 2, where processing is allocated first to the yellow wavelength followed by the red wavelength. It is worth mentioning that no mobile units were allocated blue or green wavelengths in scenario 2, and all mobile units in scenario 3 were allocated the red wavelength. This explains the zero utilization for these wavelengths, in figure 12*c*,*d*.

5. Conclusion and future work

In this paper, an OWC system was used to support multiple users. A WDMA scheme was used to support multiple users served simultaneously by the OWC system. A MILP model was developed and used to optimize resource allocation and was shown to increase the system throughput and allow MA. Thereafter, a cloud/fog-integrated architecture was built to create a connection with potential mobile nodes and to provide processing services for these mobile nodes. The mobile OW nodes were also clustered as fog mini servers and were thus also able to provide processing services to each other. A second MILP model was proposed to optimize the processing

placement by minimizing the total power consumption. Future areas of work can include (i) consideration of the uplink as the current work only considered the downlink; (ii) consideration of additional wavelengths for multi-user support enabled through infrared and WDM for example. In the current system, MA using WDM was limited by the four wavelengths available in VLC; (iii) consideration of additional MA dimensions beyond wavelengths. These can include TDM, OFDMA, orthogonal coding, spatial diversity and beam steering, which can reduce interference between users; (iv) consideration and minimization of latency in addition to the minimization of power consumption when allocating resources and placing processing jobs; (v) development of heuristics building on the MILPs insights to enable real-time resource allocation and task placement; and (vi) additionally, as this is a new integration between OW and fog computing, more work is needed to address virtualization, the software matching problem (where only a subset of the processing nodes have the relevant software for task placement), handover and quality of provided services. Also, more opportunistic scenarios need to be evaluated with other forms of fog computing.

Data accessibility. All data are provided in full in the results section of this paper.

Authors' contributions. J.M.H.E. conceived the concept and suggested the multiple access MILP optimization and processing optimization and improved the models and results. O.Z.A. and M.T.A. developed the optical wireless channel models and optical wireless channel modelling tool, obtained the optical power and interference results. S.O.M.S. developed the wavelength and AP resource optimization MILP and results. A.A.A. developed the network architecture and processing placement optimization MILP and results to minimize power consumption. S.H.M. and T.E.H.E.-G. helped with the development of the two MILP models and verified them.

Competing interests. We declare we have no competing interests.

Funding statement. This work was supported by the Engineering and Physical Sciences Research Council (ESPRC), INTERNET (EP/H040536/1), STAR (EP/K016873/1) and TOWS (EP/S016570/1) projects. The authors extend their appreciation to the deanship of Scientific Research under the International Scientific Partnership Program ISPP at King Saud University, Kingdom of Saudi Arabia, for funding this research work through ISPP#0093.

Acknowledgements. O.Z.A. thanks Umm Al Qura university in the Kingdom of Saudi Arabia for funding his PhD scholarship, A.A.A. thanks the Imam Abdulrahman Bin Faisal University in the Kingdom of Saudi Arabia for funding her PhD scholarship, S.O.M.S. thanks the University of Leeds and the Higher Education Ministry in Sudan for funding her PhD scholarship. S.H.M. thanks EPSRC for providing her Doctoral Training Award scholarship.

References

1. Mobile C. Cisco Visual Networking Index: Global Mobile Data Traffic Forecast Update, 2016–2021 White Paper [Internet]. Cisco. 2017, 1–35p. See https://www.cisco.com/c/en/us/solutions/collateral/service-provider/visual-networking-index-vni/mobile-white-paper-c11-520862.pdf%0Ahttps://www.cisco.com/c/en/us/solutions/collateral/service-provider/visual-networking-index-vni/mobile-white-paper-c11-5208.
2. Ghassemlooy Z, Popoola W, Rajbhandari S. 2013 *Optical wireless communications: system and channel modelling with Matlab*, 513 p. Boca Raton, FL: Taylor & Francis Group, LLC.
3. Alsaadi FE, Alhartomi MA, Elmirghani JMH. 2013 Fast and efficient adaptation algorithms for multi-gigabit wireless infrared systems. *J. Lightwave Technol.* **31**, 3735–3751. (doi:10.1109/JLT.2013.2286743)
4. Hussein AT, Elmirghani JMH. 2015 10 Gbps mobile visible light communication system employing angle diversity, imaging receivers, and relay nodes. *J. Opt. Commun. Netw.* **7**, 718. (doi:10.1364/JOCN.7.000718)
5. Younus SH, Elmirghani JMH. 2017 WDM for high-speed indoor visible light communication system. In *2017 19th Int. Conf. on Transparent Optical Networks (ICTON), Girona, 2017*, pp. 1–6.
6. Hussein AT, Alresheedi MT, Elmirghani JMH. 2015 20 Gb/s mobile indoor visible light communication system employing beam steering and computer generated holograms. *J. Lightwave Technol.* **33**, 5242–5260. (doi:10.1109/JLT.2015.2495165)

7. Hussein AT, Alresheedi MT, Elmirghani JMH. 2016 25 Gbps mobile visible light communication system employing fast adaptation techniques. In *Int. Conf. on Transparent Optical Networks*.
8. Alsulami OZ, Alresheedi MT, Elmirghani JMH. 2019 Transmitter Diversity with Beam Steering. In *2019 21st Int. Conf. on Transparent Optical Networks (ICTON), Angers, France, 2019*, pp. 1–5.
9. Alsulami OZ, Musa MOI, Alresheedi MT, Elmirghani JMH. 2019 Visible Light Optical Data Centre Links. In *2019 21st Int. Conf. on Transparent Optical Networks (ICTON), Angers, France, 2019*, pp. 1–5.
10. Sterckx KL, Elmirghani JMH, Cryan RA. 2000 Sensitivity assessment of a three-segment pyramidal fly-eye detector in a semidisperse optical wireless communication link. *IEE Proc.: Optoelectron.* **147**, 286–294. (doi:10.1049/ip-opt:20000609)
11. Al-Ghamdi AG, Elmirghani JMH. 2003 Performance evaluation of a triangular pyramidal fly-eye diversity detector for optical wireless communications. *IEEE Commun. Mag.* **41**, 80–86. (doi:10.1109/MCOM.2003.1186549)
12. Alresheedi MT, Elmirghani JMH. 2015 Hologram selection in realistic indoor optical wireless systems with angle diversity receivers. *J. Opt. Commun. Netw.* **7**, 797. (doi:10.1364/JOCN.7.000797)
13. Hussein AT, Alresheedi MT, Elmirghani JMH. 2016 Fast and efficient adaptation techniques for visible light communication systems. *IEEE/OSA J. Opt. Commun. Netw.* **8**, 382–397. (doi:10.1364/JOCN.8.000382)
14. Younus SH, Al-Hameed AA, Hussein AT, Alresheedi MT, Elmirghani JMH. 2019 Parallel data transmission in indoor visible light communication systems. *IEEE Access* **7**, 1126–1138. (doi:10.1109/ACCESS.2018.2886398)
15. Al-Ghamdi A, Elmirghani JMH. 2003 Optimisation of a PFDR antenna in a fully diffuse OW system influenced by background noise and multipath propagation. *IEEE Trans. Commun.* **51**, 2103–2114. (doi:10.1109/TCOMM.2003.820758)
16. Al-Ghamdi AG, Elmirghani JMH. 2004 Characterization of mobile spot diffusing optical wireless systems with receiver diversity. In *ICC'04 IEEE Int. Conf. on Communications*.
17. Alsaadi FE, Elmirghani JMH. 2009 Performance evaluation of 2.5 Gbit/s and 5 Gbit/s optical wireless systems employing a two dimensional adaptive beam clustering method and imaging diversity detection. *IEEE J. Sel. Areas Commun.* **27**, 1507–1519. (doi:10.1109/JSAC.2009.091020)
18. Alsulami OZ, Alresheedi MT, Elmirghani JMH. 2019 Optical Wireless Cabin Communication System. In *2019 IEEE Conf. on Standards for Communications and Networking (CSCN), Granada, Spain, 2019*, pp. 1–4.
19. Alsulami OZ, Musa MOI, Alresheedi MT, Elmirghani JMH. 2019 Co-existence of Micro, Pico and Atto Cells in Optical Wireless Communication. In *2019 IEEE Conf. on Standards for Communications and Networking (CSCN), Granada, Spain, 2019*, pp. 1–5.
20. Alresheedi MT, Elmirghani JMH. 2012 10 Gb/s indoor optical wireless systems employing beam delay, power, and angle adaptation methods with imaging detection. *IEEE/OSA J. Lightwave Technol.* **30**, 1843–1856. (doi:10.1109/JLT.2012.2190970)
21. Sterckx KL, Elmirghani JMH, Cryan RA. 1999 Pyramidal Fly-Eye Detection Antenna for Optical Wireless Systems. In *Digest IEE Colloq. on Optical Wireless Communications. Digest No. 1999: 5/1–5/6*.
22. Alsaadi FE, Esfahani MN, Elmirghani JMH. 2010 Adaptive mobile optical wireless systems employing a beam clustering method, diversity detection and relay nodes. *IEEE Trans. Commun.* **58**, 869–879. (doi:10.1109/TCOMM.2010.03.080361)
23. Alsaadi FE, Elmirghani JMH. 2009 Adaptive mobile line strip multibeam MC-CDMA optical wireless system employing imaging detection in a real indoor environment. *IEEE J. Sel. Areas Commun.* **27**, 1663–1675. (doi:10.1109/JSAC.2009.091216)
24. Alresheedi MT, Elmirghani JMH. 2011 Performance evaluation of 5 Gbit/s and 10 Gbit/s mobile optical wireless systems employing beam angle and power adaptation with diversity receivers. *IEEE J. Sel. Areas Commun.* **29**, 1328–1340. (doi:10.1109/JSAC.2011.110620)
25. Alsaadi FE, Elmirghani JMH. 2011 Mobile multi-gigabit indoor optical wireless systems employing multibeam power adaptation and imaging diversity receivers. *IEEE/OSA J. Opt. Commun. Networking* **3**, 27–39. (doi:10.1364/JOCN.3.000027)

26. Al-Ghamdi AG, Elmirghani JMH. 2004 Line strip spot-diffusing transmitter configuration for optical wireless systems influenced by background noise and multipath dispersion. *IEEE Trans. Commun.* **52**, 37. (doi:10.1109/TCOMM.2003.822160)
27. Alsaadi FE, Elmirghani JMH. 2010 High-speed spot diffusing mobile optical wireless system employing beam angle and power adaptation and imaging receivers. *J. Lightwave Technol.* **28**, 2191–2206. (doi:10.1109/JLT.2010.2042140)
28. Cossu G, Khalid AM, Choudhury P, Corsini R, Ciaramella E. 2012 3.4 Gbit/s visible optical wireless transmission based on RGB LED. *Opt. Express* **20**, B501–B506. (doi:10.1364/OE.20.00B501)
29. Wang Y, Wang Y, Chi N, Yu J, Shang H. 2013 Demonstration of 575-Mb/s downlink and 225-Mb/s uplink bi-directional SCM-WDM visible light communication using RGB LED and phosphor-based LED. *Opt. Express* **21**, 1203. (doi:10.1364/OE.21.001203)
30. Neumann A, Wierer JJ, Davis W, Ohno Y, Brueck SRJ, Tsao JY. 2011 Four-color laser white illuminant demonstrating high color-rendering quality. *Opt. Express* **19**(S4), A982. (doi:10.1364/OE.19.00A982)
31. Wu F-M, Lin C-T, Wei C-C, Chen C-W, Chen Z-Y, Huang K. 2013 3.22-Gb/s WDM Visible Light Communication of a Single RGB LED Employing Carrier-Less Amplitude and Phase Modulation. In *Optical Fiber Communication Conf./National Fiber Optic Engineers Conf. 2013 2013*, p. OTh1G.4. See https://www.osapublishing.org/abstract.cfm?uri=OFC-2013-OTh1G.4.
32. Khan TA, Tahir M, Usman A. 2012 Visible light communication using wavelength division multiplexing for smart spaces. In *Consumer Communications and Networking Conference (CCNC)*, 2012, pp. 230–234. IEEE.
33. Shaukat U, Ahmed E, Anwar Z, Xia F. 2016 Cloudlet deployment in local wireless networks: motivation, architectures, applications, and open challenges. *J. Netw. Comput. Appl.* **62**, 18–40. (doi:10.1016/j.jnca.2015.11.009)
34. Yousefpour A, Fung C, Nguyen T, Kadiyala K, Jalali F, Niakanlahiji A *et al.* 2019 All one needs to know about fog computing and related edge computing paradigms: a complete survey. *J. Syst. Archit.* **98**, 289–330. (doi:10.1016/j.sysarc.2019.02.009)
35. Shi W, Cao J, Zhang Q, Li Y, Xu L. 2016 Edge computing: vision and challenges. *IEEE Internet Things J.* **3**, 637–646. (doi:10.1109/JIOT.2016.2579198)
36. Witkowski M, Brenner P, Jansen R, Go DB, Ward E. 2010 Enabling sustainable clouds via environmentally opportunistic computing. In *Proceedings - 2nd IEEE Int. Conf. on Cloud Computing Technology and Science, CloudCom 2010, 2010*, pp. 587–592.
37. Kuada E, Olesen H. 2012 Incentive Mechanism design for Opportunistic Cloud Computing Services. In *Collaborative Computing: Networking, Applications and Worksharing (CollaborateCom), 2012 8th Int. Conf. 2012*, p. 127–136. See http://ieeexplore.ieee.org/ielx5/6415460/6450881/06450900.pdf?tp=&arnumber=6450900&isnumber=6450881%5Cnhttp://ieeexplore.ieee.org/xpls/abs_all.jsp?arnumber=6450900&tag=1.
38. Peralta G, Iglesias-Urkia M, Barcelo M, Gomez R, Moran A, Bilbao J. 2017 Fog computing based efficient IoT scheme for the Industry 4.0. In *Proc. 2017 IEEE Int Work Electron Control Meas Signals their Appl to Mechatronics, ECMSM 2017. 2017;1–6*.
39. Olariu S, Khalil I, Abuelela M. 2011 Taking VANET to the clouds. *Int. J. Pervasive Comput. Commun.* **7**, 7–21. (doi:10.1108/17427371111123577)
40. Miluzzo E, Cáceres R, Chen Y-F. 2012 Vision mClouds – Computing on Clouds of Mobile Devices. In *Proc. of the third ACM workshop on Mobile cloud computing and services - MCS '12. 2012*, p. 9. See http://dl.acm.org/citation.cfm?doid=2307849.2307854.
41. Hasan R, Khan R. 2016 A Cloud You Can Wear: Towards a Mobile and Wearable Personal Cloud. In *Proc. - Int. Computer Software and Applications Conference 2016* [cited 2018 January 31], p. 823–828. See https://pdfs.semanticscholar.org/bedd/b98bb46f57609196fb3901beb907e430f3b4.pdf.
42. Chen M-H, Dong M, Liang B. 2018 Resource Sharing of a Computing Access Point for Multi-user Mobile Cloud Offloading with Delay Constraints. Retrieved from https://arxiv.org/pdf/1712.00030.pdf.
43. Rahimi MR, Venkatasubramanian N, Mehrotra S, Vasilakos AV. 2012 MAPCloud: Mobile applications on an elastic and scalable 2-tier cloud architecture. In *Proc. - 2012 IEEE/ACM 5th Int. Conf. on Utility and Cloud Computing, UCC 2012*, pp. 83–90. See https://doi.org/10.1109/UCC.2012.25.

44. Jalali F, Hinton K, Ayre R, Alpcan T, Tucker RS. 2016 Fog computing may help to save energy in cloud computing. *IEEE J. Sel. Areas Commun.* **34**, 1728–1739. (doi:10.1109/JSAC.2016.2545559)
45. Alresheedi MT, Hussein AT, Elmirghani JMH. 2016 Uplink design in VLC systems with IR sources and beam steering. *IET Commun.* **11**, 311–317. (doi:10.1049/iet-com.2016.0495)
46. Alsulami OZ, Alresheedi MT, Elmirghani JMH. 2019 Infrared uplink design for visible light communication (VLC) systems with beam steering. In *2019 IEEE Int. Conf. on Computational Science and Engineering (CSE) and IEEE Int. Conf. on Embedded and Ubiquitous Computing (EUC), New York, NY, USA, 2019*, pp. 57–60.
47. Saeed SOM, Mohamed SH, Alsulami OZ, Alresheedi MT. 2019 Elmirghani JMH. "Optimized Resource Allocation in Multi-User WDM VLC Systems. In *2019 21st Int. Conf. on Transparent Optical Networks (ICTON), Angers, France, 2019*, pp. 1–5.
48. Gfeller FR, Bapst U. 1979 Wireless in-house data communication via diffuse infrared radiation. *Proc. IEEE* **67**, 1474–1486. (doi:10.1109/PROC.1979.11508)
49. Hussein AT, Elmirghani JMH. 2015 Mobile multi-gigabit visible light communication system in realistic indoor environment. *J. Light Technol.* **33**, 3293–3307. (doi:10.1109/JLT.2015.2439051)
50. Barry JR, Kahn JM, Krause WJ, Lee EA, Messerschmitt DG. 1993 Simulation of multipath impulse response for indoor wireless optical channels. *IEEE J. Sel. Areas Commun.* **11**, 367–379. (doi:10.1109/49.219552)
51. Personick SD. 1973 Receiver design for digital fiber optic communication systems, I & II. *Bell Syst. Tech. J.* **52**, 875–886. (doi:10.1002/j.1538-7305.1973.tb01994.x)
52. Moreira A, Valadas R, de Oliveira Duarte AM. 1997 Optical interference produced by artificial light. *Wireless Netw.* **3**, 131–140. (doi:10.1023/A:1019140814049)
53. Hadi MS, Lawey AQ, El-Gorashi TEH, Elmirghani JMH. 2019 Patient-centric cellular networks optimization using big data analytics. *IEEE Access* **7**, 49 279–49 296. (doi:10.1109/ACCESS.2019.2910224)
54. Dong X, El-Gorashi T, Elmirghani J. 2011 Green IP over WDM networks with data centers. *J. Lightwave Technol.* **29**, 1861–1880. (doi:10.1109/JLT.2011.2148093)
55. Ali HMM, Lawey AQ, El-Gorashi TEH, Elmirghani JMH. 2017 Future energy efficient data centers with disaggregated servers. *IEEE/OSA J. Lightwave Technol.* **35**, 5361–5380. (doi:10.1109/JLT.2017.2767574)
56. Musa M, El-Gorashi TEH, Elmirghani JMH. 2018 Bounds on GreenTouch GreenMeter network energy efficiency. *IEEE/OSA J. Lightwave Technol.* **36**, 5395–5405. (doi:10.1109/JLT.2018.2871602)
57. Lawey AQ, El-Gorashi TEH, Elmirghani JMH. 2014 BitTorrent content distribution in optical networks. *IEEE/OSA J. Lightwave Technol.* **32**, 3607–3623. (doi:doi:10.1109/jlt.2014.2351074)
58. Nonde L, El-Gorashi TEH, Elmirghani JMH. 2015 Energy efficient virtual network embedding for cloud networks. *IEEE/OSA J. Lightwave Technol.* **33**, 1828–1849. (doi:10.1109/JLT.2014.2380777)
59. Al-Quzweeni AN, Lawey AQ, El-Gorashi TEH, Elmirghani JMH. 2019 Optimized energy aware 5G network function virtualization. *IEEE Access* **7**, 44 939–44 958. (doi:10.1109/ACCESS.2019.2907798)
60. Bathula B, Alresheedi M, Elmirghani JMH. 2009 Energy efficient architectures for optical networks. In *Proc. IEEE London Communications Symposium*.
61. Musa M, El-Gorashi TEH, Elmirghani JMH. 2018 Bounds for energy-efficient survivable IP Over WDM networks with network coding. *IEEE/OSA J. Opt. Commun. Networking.* **10**, 471–481. (doi:10.1364/JOCN.10.000471)
62. Musa M, El-Gorashi TEH, Elmirghani JMH. 2017 Energy efficient survivable IP-over-WDM networks with network coding. *IEEE/OSA J. Opt. Commun. Networking.* **9**, 207–217. (doi:10.1364/JOCN.9.000207)
63. Bathula B, Elmirghani JMH. 2009 Energy Efficient Optical Burst Switched (OBS) Networks. In *IEEE GLOBECOM 09*.
64. Dong X, El-Gorashi TEH, Elmirghani JMH. 2014 Green optical OFDM networks. *IET Optoelectron.* **8**, 137–148. (doi:10.1049/iet-opt.2013.0046)
65. Osman NI, El-Gorashi TEH, Krug L, Elmirghani JMH. 2014 Energy efficient future high-definition TV. *J. Lightwave Technol.* **32**, 2364–2381. (doi:10.1109/JLT.2014.2324634)

66. Dong X, El-Gorashi TEH, Elmirghani JMH. 2011 IP over WDM networks employing renewable energy sources. *J. Lightwave Technol.* **29**, 3–14. (doi:10.1109/JLT.2010.2086434)
67. Dong X, El-Gorashi TEH, Elmirghani JMH. 2012 On the energy efficiency of physical topology design for IP over WDM networks. *IEEE/OSA J. Lightwave Technol.* **30**, 1931–1942. (doi:10.1109/JLT.2012.2189869)
68. Al-Azez Z, Lawey A, El-Gorashi TEH, Elmirghani JMH. 2019 Energy efficient IoT virtualization framework with peer to peer networking and processing. *IEEE Access* **7**, 50 697–50 709. (doi:10.1109/ACCESS.2019.2911117)
69. Al-Salim AM, Lawey A, El-Gorashi TEH, Elmirghani JMH. 2018 Energy efficient big data networks: impact of volume and variety. *IEEE Trans. Netw. Serv. Manage.* **15**, 458–474. (doi:10.1109/TNSM.2017.2787624)
70. Al-Salim AM, Lawey A, El-Gorashi TEH, Elmirghani JMH. 2018 Greening big data networks: velocity impact. *IET Optoelectron.* **12**, 126–135. (doi:10.1049/iet-opt.2016.0165)
71. Hadi MS, Lawey A, El-Gorashi TEH, Elmirghani JMH. 2018 Big data analytics for wireless and wired network design: a survey. *Elsevier Comput. Netw.* **132**, 180–199. (doi:10.1016/j.comnet.2018.01.016)
72. 'Intel® Xeon® Processor E5-2680 v2 (25M Cache, 2.80 GHz) Product Specifications.' [Online]. See https://ark.intel.com/content/www/us/en/ark/products/75277/intel-xeon-processor-e5-2680-v2-25m-cache-2-80-ghz.html (accessed 30 January 2019).
73. 'Intel® Xeon® Processor X5675 (12M Cache, 3.06 GHz, 6.40 GT/s Intel® QPI) Product Specifications.' [Online]. See https://ark.intel.com/content/www/us/en/ark/products/52577/intel-xeon-processor-x5675-12m-cache-3-06-ghz-6-40-gt-s-intel-qpi.html (accessed 11 July 2019).
74. 'Intel® CoreTM2 Quad Processor Q9400 (6M Cache, 2.66 GHz, 1333 MHz FSB) Specifications-Essentials' [Online]. See http://ark.intel.com/products/35365/IntelCore2QuadProcessorQ94006MCache2_66GHz1333MHzFSB (accessed 27 June 2019).
75. 'Intel® Xeon® Processor E5-2420 (15M Cache, 1.90 GHz, 7.20 GT/s Intel® QPI) Product Specifications.' [Online]. See https://ark.intel.com/content/www/us/en/ark/products/64617/intel-xeon-processor-e5-2420-15m-cache-1-90-ghz-7-20-gt-s-intel-qpi.html (accessed 30 June 2019).
76. 'Intel® CoreTM i7-6500U Processor (4M Cache, up to 3.10 GHz) Product Specifications.' [Online]. See https://ark.intel.com/content/www/us/en/ark/products/88194/intel-core-i7-6500u-processor-4m-cache-up-to-3-10-ghz.html (accessed 12 July 2019).
77. Biswas M, Whaiduzzaman M. 2018 Efficient mobile cloud computing through computation offloading. *Int. J. Adv. Technol.* **10**, 2
78. Tellabs 2016 Tellabs® 1100 Series Optical Line Terminals (OLTs). See www.tellabs.com (accessed 10 January 2019).
79. S Electric. 2016 FTE7502 EPON Optical Network Unit (10G ONU) datasheet. [Online]. See http://www.sumitomoelectric.com/onu-fte7502.html (accessed 15 June 2019).
80. Lawey AQ, El-Gorashi TEH, Elmirghani JMH. 2014 Distributed energy efficient clouds over core networks. *J. Lightwave Technol.* **32**, 1261–1281. (doi:10.1109/JLT.2014.2301450)
81. Elmirghani JMH *et al.* 2018 GreenTouch GreenMeter Core network energy-efficiency improvement measures and optimization. *J. Opt. Commun. Netw.* **10**, A250. (doi:10.1364/JOCN.10.00A250)
82. EDFA. 2012 Enhanced C-Band 96-Channel EDFA amplifiers for the Cisco ONS 15454 MSTP. [Online]. See https://www.cisco.com/c/en/us/products/collateral/optical-networking/ons-15454-series-multiservice-transport-platforms/data_sheet_c78-658542.pdf (accessed 10 January 2019)
83. Cisco. 2018 Cisco 220 Series Smart Switches. See https://www.cisco.com/c/en/us/products/cloud-systems-management/small-business-findit-network- (accessed 10 January 2019).
84. Cisco. 2004 CISCO 12000 SERIES PERFORMANCE ROUTER PROCESSOR-1. See https://www.cisco.com/c/en/us/products/collateral/routers/12000-series-routers/product_data_sheet0900aecd800f4147.pdf (accessed 10 April 2019).
85. Cisco. 2017 Cisco Catalyst 6880-X Series Extensible Fixed Aggregation. See https://www.cisco.com/web/solutions/sp/vni/vni_forecast_highlights/index.html (accessed 10 January 2019).